Label-Free Study of Bovine Serum Albumin Conformational Dynamics using Optical Nanotweezers and Experimental Analysis of Asymmetric DNH Nanostructures

by

Sherin George

Bachelor of Technology, MG University, 2018

A thesis submitted in partial fulfillment of the requirements for the degree of

MASTER OF APPLIED SCIENCE

in the

Department of Electrical and Computer Engineering

University of Victoria

Supervisory Committee

Label-Free Study of Bovine Serum Albumin Conformational Dynamics using Optical Nanotweezers and Experimental Analysis of Asymmetric DNH Nanostructures

by

Sherin George

Bachelor of Technology, MG University, 2018

Supervisory committee

Dr. Reuven Gordon, **Supervisor**

Department of Electrical and Computer Engineering

Dr. Levi Smith, **Committee Member**

Department of Electrical and Computer Engineering

Abstract

This thesis concerns the label-free investigation of Bovine Serum Albumin(BSA) conformational dynamics and the interaction of different proteins with gold surfaces using Double Nanohole(DNH) optical tweezers. It is divided into two parts: Study of conformational changes of labeled and unlabelled BSA and investigation of electrostatic interactions between proteins and gold surfaces. The Gibbs energy for the N to F states was calculated for both labeled and unlabelled BSA from the free energy diagram and the values show a small effect of labeling on the protein. This Chapter also explored the effect of electrostatic interactions between the gold surface and proteins with different charges on the trapping stiffness. Further, the experimental investigation of the development of a new nanostructure called Asymmetric Double Nanohole and its possible application in optical trapping are described in this thesis. Fabrication techniques and result analysis are described, even though the trapping efficiency turned out to be the same as that for traditional DNH structures.

Contents

List of Figures

Acknowledgements

I would like to extend my deepest gratitude to my supervisor, Professor **Reuven Gordon**, for providing me with the opportunity to work at the cutting edge of plasmonics research and for his invaluable guidance throughout my academic journey.

I am also incredibly thankful to my collaborators and colleagues in the Nanoplasmonics Research Group, including **Dr. Demelza Wright, Dr. Veerpal Kaur, Elham Babaei,Elham Hosseini, Behnam Khosravi, Matthew Peters, Annie Yang, Tianyu Zhang, and Keiran Letwin**, for their continuous encouragement, valuable discussions, and friendship.

I owe a special thanks to the faculty and staff at the **Centre for Advanced Materials and Related Technology (CAMTEC)** and the **Advanced Microscopy Facility (AMF)** for their training and support throughout my research.

Finally, to my **family and friends**, your unconditional love, encouragement, and support have been my foundation through this journey, and for that, I am forever grateful.

"If you fail, never give up. F.A.I.L. stands for 'First Attempt In Learning.' If you get No as an answer, remember N.O. means 'Next Opportunity'."

— A.P.J. Abdul Kalam

Dedicated to...

To all the researchers embarking on this challenging journey...

Chapter 1

Introduction

The ability of light to exert forces has been known since at least 1619. Forces of radiation pressure from a laser beam can be used to accelerate and trap freely suspended particles as discovered by Ashkin in the 1970s. He proved that if a laser beam of power in the range of milliwatts hits a microscopic sphere off-center it draws the sphere into the beam and that the sphere is accelerated in the direction of propagation of light [1]. In 1986, Ashkin Arthur showed that a single laser beam can be used to trap and manipulate microscopic particles [2] and in the following year optical trapping of bacteria, tobacco mosaic virus, and red blood cells were successfully demonstrated [3] [4].

1.1 Motivation

1.1.1 Label-Free Study of BSA Conformational Dynamics

The ability to understand and control protein dynamics is critical for advances in fields ranging from biophysics to drug development. The free-energy landscape is fundamentally a graph depicting energy along a reaction coordinate, which describes molecular biophysics at the single-molecule level. Conformational dynamics demonstrate pathways on the energy landscape, significantly influencing protein function. Single molecule techniques are preferred for seeing these dynamics, and typical methods for investigating proteins at the single molecule level utilize labels or tethers. Although these methods have proven greatly effective, they require the incorporation of a label or tether, which entails additional procedures and possibly changes to the protein's inherent function. Consequently, methods capable of directly observing the dynamics of unaltered protein conformations at the single-molecule level are desired. The conformational dynamics of a single unmodified protein have been largely unexplored, and this study intends to investigate these dynamics in a single unmodified BSA protein utilizing DNH optical tweezers.

1.1.2 Electrostatic Interactions between Proteins and Gold Surface

Proteins often engage with surfaces in both biological and technological settings. Electrostatic interactions could influence protein behavior in proximity to these surfaces. Gold is frequently utilized in biosensors, especially in applications involving Surface Plasmon Resonance (SPR). In optical tweezer studies, the interaction between proteins and the trapping substrate, such as gold, can affect trapping efficiency. The electrostatic repulsion or attraction between proteins and gold can either facilitate or impede the trapping process. In DNH optical tweezers, the DNH is constructed on a gold surface, and a preliminary investigation into the interactions of several proteins with differing charges on the gold surface is conducted to better understand this mechanism.

1.1.3 Asymmetric DNHs: A Experimental Study

To improve the flexibility and efficiency in trapping different molecules different nanostructures must be studied. The efficacy of DNH optical tweezers is attributed to their capacity to capture diminutive proteins. DNHs have a significant field gradient within a region comparable to the dimensions of the particle, resulting in large optical forces that enable stable trapping and sizing of significantly smaller proteins. Exploring new nanostructures such as the Asymmetric Double Nanohole (ADNH) opens possibilities for more efficient trapping mechanisms and improved detection sensitivity. By conducting experimental studies on ADNHs, this thesis aims to provide new insights into the performance and potential applications of such nanostructures in optical trapping setups.

1.1.4 Classification of Lipopolysaccharides using DNH Optical Tweezers: Ongoing project

This study is motivated by the essential role of lipopolysaccharides (LPS) in bacterial pathogenicity and their considerable effects on human health. LPS are powerful inflammatory chemicals located on the outer membrane of these bacteria. Also called endotoxins, they are key triggers of inflammation and immune responses, often leading to severe conditions such as sepsis. The ability to analyze and differentiate LPS types could enhance the precision of bacterial detection and contribute to advancements in biomedical applications. The project focuses on distinguishing between four types of LPS using DNH optical tweezers however, this thesis currently includes findings from only two, as data collection for the remaining species is still underway. Further experiments and analyses are needed to complete the comprehensive evaluation of all four LPS types.

1.2 Thesis Organization

This section gives an outline of the thesis chapters with a short description of their contents.

Chapter 2 discusses the theoretical foundation of plasmonics, optical tweezers, and subwavelength apertures. It highlights the advantages of DNH tweezers over conventional optical tweezers, emphasizing their enhanced trapping capabilities.

Chapter 3 provides a detailed explanation of the experimental setup for the DNH aperture tweezer, including the fabrication process of the DNH and the assembly of the chip, which is consistently used throughout the experiments in this thesis.

Chapter 4 is divided into two parts. The first part explores the conformational dynamics of a single, unmodified BSA molecule using the free-energy landscape approach, a study in which I actively participated. The second part examines the influence of electrostatic interactions between the gold surface and proteins on the trapping behavior.

Chapter 5 introduces a novel nanostructure: the ADNH. It covers the fabrication procedures and provides an analysis of the results obtained from the exploration of this structure.

Chapter 6 gives a brief overview of ongoing research focused on classifying single LPS molecules using DNH optical tweezers. The study aims to distinguish four different LPS types by leveraging the optical trapping characteristics of DNH structures.

Chapter 7 concludes the thesis and describes possibilities for future work.

1.3 Author's Contribution

1. The work presented in Chapter 4 ”Conformational Changes in Unlabelled and Labeled BSA” is published in npj biosensing.

   Peters, M. et al. (2024) ‘Energy Landscape of Conformational Changes for a Single Unmodified Protein’, Research Square [Preprint].

   The author contributed by providing critical trapping events at different power levels for the experiments.

2. The effect of electrostatic Interactions between proteins of different charges and gold surface on trapping efficiency were studied.
3. A novel nanostructure, ADNH was fabricated and tested for optical trapping.
4. The optical trapping and differentiation of two LPS were performed using DNH optical tweezers.

Chapter 2

Theory

This chapter overviews the basic principles and applications of single-beam gradient force optical tweezers, a popular tool for manipulating microscopic particles using focused laser beams. Traditional optical tweezers, while very successful in the biological and physical sciences, do have some disadvantages. Among them are the trapping of nanoscale objects or low-refractive-index particles. More recently, these issues have been bypassed by aperture-based optical traps, where these devices leverage effects like extraordinary optical transmission through subwavelength apertures at a higher trapping efficiency. The DNH structure has, so far, been a widely used geometry in the demonstration of particle trapping in the nanoscale, since its near-field enhancements are intense. Apart from introducing nanoaperture-based traps, this chapter will also describe such a concept as so-called Self Induced Back Action (SIBA) trapping, where the target particles take an active role in the trapping dynamics and open new possibilities for highly efficient and stable trapping at the nanoscale. This Chapter will show how these advanced trapping mechanisms overcome the traditional limitations of optical tweezers and ultimately enable new avenues of research in nanophotonics and biophysics.

2.1 Conventional Optical Tweezers

Optical Tweezers are based on the fact that light carries energy and momentum even though it has zero mass. Optical traps are formed by tightly focusing a laser beam using a high numerical aperture (NA) objective lens. When light is incident on dielectric particles, the transfer of momentum between photons induces a force on the particle. This force can be divided into scattering force, in the direction of incident light, and gradient force, acting in the direction of intensity gradient of light. The trap is stable because the gradient force, which pulls the particle to the high focus of the beam presides over the scattering force which pushes it away [1]. This condition demands a tightly focused trapping laser beam to be directed to a diffraction-limited area using a high NA objective, causing a steep gradient in the light. The axial equilibrium position of a confined particle in the trap is slightly out of the focal point due to the equilibrium between the gradient force and the scattering force. The gradient force acts as a restoring force when the particle moves away from the equilibrium position, thus the trap acts like a Hookean spring [5] and can be characterized by a spring constant k:

$$F = -kx \tag{2.1}$$

where x is the displacement of the particle from the equilibrium.

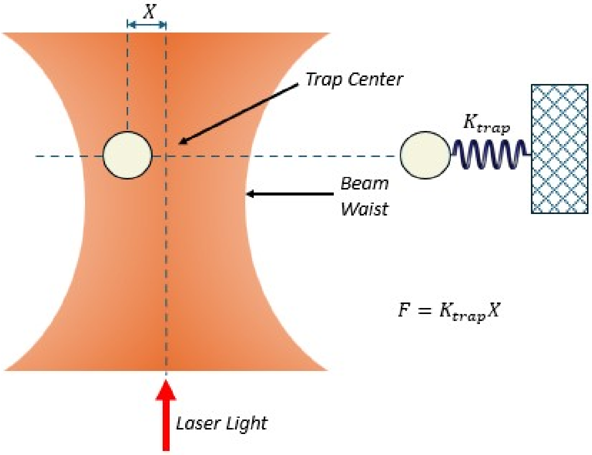

Figure 2.1: Optical trap obeys Hooke's Law.

The optical trapping forces are calculated for two cases. Mie scattering is dominant for particles whose size is larger than the wavelength of the laser $r >> \lambda$. Force can be calculated in terms of geometric ray optics as the particle acts as a refractive object. For particles whose size is smaller than the laser wavelength employed as the source of trapping $r << \lambda$, Rayleigh scattering is satisfied and the trapping force can be computed by treating the particle as a point dipole with an induced dipole momentum [5] [6].

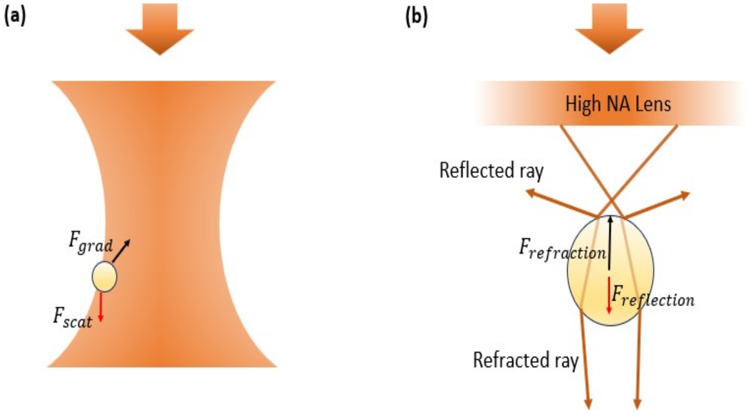

Figure 2.2: Forces on a dielectric sphere interacting with highly focused light beam (a) A Rayleigh particle experiences a scattering force (F_{scat}) that pushes the particle along the direction of propagation of the light and a gradient force (F_{grad}) that attracts it towards the focus. (b)A dielectric sphere larger than the wavelength of light either reflects or refracts light. The incident light refracted by the particle gains forward momentum which generates $F_{refraction}$ that pulls the bead towards the focus. Conversely, the reflected light loses forward momentum, pushing the bead forward with a force $F_{reflection}$.

2.2 Brief Review of Optical Trapping Forces in Rayleigh Regime

By employing the Dipole Approximation to calculate the optical force, the time-averaged force is given by [7] [8],

$$\langle F\rangle = \frac{1}{4}\Re(\alpha_p)\nabla E^2 + \frac{\sigma(\alpha_p)}{2c}\Re(E\times H^*) + \sigma(\alpha_p)c\nabla\times(\frac{\varepsilon_0}{4\omega i}E\times E^*) \tag{2.2}$$

where $\langle..\rangle$ represents time averaged operation, $\Re$ is the real part, α_p is the polarisability, E and H are the Electric and Magnetic field vectors respectively, c is the speed of light in vacuum, ε_0 is the vacuum dielectric permittivity and ω is the angular frequency of the optical field. The polarisability α_p of the small dielectric particle is given by

$$\alpha_p = \frac{\alpha_0}{1 - i\alpha_0 k_0^3/6\pi\varepsilon_0} \tag{2.3}$$

where k is the wavenumber and α_0 is the Clausius-Mossotti relation[9]

$$\alpha_0 = 4\pi n_m^2 \varepsilon_0 r^3 \frac{m^2 - 1}{m^2 + 2} \tag{2.4}$$

where m is the relative refractive index of the particle compared to its surrounding medium,$m = \frac{n_p}{n_m}$, where n_p is the refractive index of the particle, n_m is the refractive index of the surrounding medium and r is the radius of the particle [10]. The first term in Eq (2.2) represents the gradient force that attracts the particle along the direction of the increasing electric field intensity gradient. The second term gives the scattering force or the radiation force that pushes the particle away. The third is the “spin curl force,” which arises from the presence of the spatial polarization gradients. This force is nonzero for a tightly focused beam in an optical tweezer[8]. However, linearly polarized light does not carry spin angular momentum, as spin angular momentum is associated with circular or elliptical polarization. As a result, the spin-curl force dependent is also zero, regardless of how tightly the beam is focused. Therefore, in an optical tweezer setup using linearly polarized light, the third term does not contribute to the overall force. The interplay of the aforementioned forces establishes an equilibrium point near the laser focus, facilitating three-dimensional optical trapping.

The scattering forces, given by the second and third terms in Eq (2.2), are both proportional to the cross-section of the particle, $\sigma(\alpha_p)$, which is also a function of the polarizability, α_p. The total cross-section of the particle is the sum of the absorption and scattering cross-sections given by:

$$\sigma(\alpha_p) = \sigma_{sc}(\alpha_p) + \sigma_{abs}(\alpha_p) \tag{2.5}$$

$$\sigma_{sc} = \frac{k^4}{6\pi\varepsilon_0^2}|\alpha_p|^2 \tag{2.6}$$

where the scattering cross-section is proportional to the absolute square of the polarizability.

$$\sigma_{abs} = \frac{k}{\varepsilon_0}\Im(\alpha_p)$$

and the absorption cross-section is proportional to the imaginary component of the polarizability ($\Im(\alpha_p)$) only. The scattering cross-section determines the amount of light scattered by the particle. In dielectric materials, this term predominates the overall cross-section. A substantial scattering cross-section generates a considerable radiation pressure force that destabilizes the optical trap by displacing the particle in the direction of beam propagation. σ_{abs} provides information on the amount of energy absorbed by the particle and is directly related to the associated temperature increase [11]. If the absorption cross-section is sufficiently large to considerably raise the temperature of the particle, the resultant increase in Brownian motion demands a greater gradient force to trap the particle. For a particle to be trapped in an optical tweezer, the axial component of the gradient force must exceed the destabilizing effects of the scattering force. The scattering force is proportional to the scattering cross-section. Equating Eq(2.3) in to Eq(2.6) we get,

$$\sigma_{sc} = r^6 \frac{128\pi^5}{3\pi^4} (\frac{m^2 - 1}{m^2 + 2})^2 \tag{2.7}$$

Here the scattering force is proportional to r^6.The scattering force is insignificant for small particles but rises quickly with increasing particle size, causing larger particles to be displaced from the focal volume of optical tweezers. This establishes an upper limit on the maximum particle size that can be confined within an optical trap [8].

From Eq (2.2),

$$F_{grad} = \frac{1}{4} \Re(\alpha_p) \nabla \langle |E|^2 \rangle \tag{2.8}$$

Inserting Eq(2.3),the simplified expression for the polarizability, valid for dielectric particles into the relation for the gradient force given in Eq(2.8), we get

$$F_{grad} = r^3 \pi n_m^2 \varepsilon_0 (\frac{m^2 - 1}{m^2 + 2}) \nabla \langle |E|^2 \rangle \tag{2.9}$$

Hence, the gradient force exerted on a trapped particle is proportional to the third power of the particle radius, that is, r^3.Consequently, nanoparticles are challenging to optically trap because the gradient force may be inadequate to establish a trap deep enough to counteract the particle's Brownian motion; larger particles suffer a significantly greater gradient force compared to smaller particles [2] [10]. In addition, to achieve steady trapping of a nanoparticle, the trapping potential generated by optical forces must overcome the thermal energy. The trapping potential on a particle at r_0 is given by

$$U(r_0) = \int_{\infty}^{r_0} F(r)\, dr$$

For stable trapping, the depth of this potential well must be approximately $10K_BT$ (where K_B is Boltzmann's constant and T denotes the absolute temperature of the trap) to counteract the particle's delocalization caused by Brownian motion [12]. However, this is difficult to achieve for small particles and is a limitation of conventional gradient force optical tweezers.

Another force that can be taken into account is given by Stoke's Law. This law states that the force on a sphere of radius r moving through a fluid with viscosity η at a velocity v is directly proportional to the radius of the particle.

$$F_s = 6\pi r\eta v \tag{2.10}$$

The frictional coefficient γ is given by Stokes' law for a spherical particle as

$$\gamma = 6\pi\eta r$$

As the particle size decreases, the thermal motion of the particle increases, and the force on the particle becomes weak. Therefore, to confine a nanoparticle using the gradient force requires either an increase in the light field intensity or that one works with highly polarizable particles. However, these requirements are not feasible for small biological specimens such as proteins and DNA strands, since they are temperature sensitive. Numerous studies have employed optical trapping to manipulate individual proteins, DNA, and RNA by tethering them to larger dielectric beads. These beads serve as "handles," enabling precise control and manipulation of the biomolecules, as the optical trap exerts forces on the beads, indirectly influencing the attached molecules [13] [14] [15]. However, many proteins are significantly smaller than the dielectric beads typically used in optical trapping experiments, and thus the measurements may not accurately capture the protein's intrinsic behavior. The large size of the bead can alter the dynamics of the protein, influencing its diffusion, rotation, and conformational changes. This discrepancy can lead to artifacts in the data, as the bead's mass and interaction with the surrounding medium may overshadow the native biophysical properties of the smaller protein. To overcome these limitations, nanoapertures in metal films or plasmonic nanostructures were developed for trapping and studying small proteins. These nanostructures can create highly localized fields for trapping smaller objects without requiring large dielectric beads.

2.3 Subwavelength Apertures

Subwavelength Aperture refers to an aperture in a metal film of size much smaller than the wavelength of light. When light strikes an aperture in a metal film that is smaller than the wavelength of the light, it cannot propagate through the aperture as light with a large wavelength cannot "fit" itself into a much smaller hole. The tangential electric field must be zero at the metal surface for a perfect conductor. Light gets diffracted at the edge of the aperture due to the inability of propagating waves to satisfy the boundary conditions. Hans Bethe first studied the transmission of light through a circular hole with a diameter much smaller than the wavelength on an infinite perfect electric conductor (PEC) plane [16]. With plane wave incident normally to the PEC plane and the electric and magnetic field parallel to the PEC plane, the light transmitted through the circular aperture is approximated by the emission of a magnetic dipole. The transmitted power through the hole can be expressed as the power emitted by this dipole.

$$T = \frac{1}{2}(\frac{4Z_0\pi^3}{3\lambda_0^4})(\frac{8r^3}{3}H_0)^2 \propto \frac{r^6}{\lambda^4} \tag{2.11}$$

where Z_0 is the free-space impedance, $\lambda_0$is the wavelength in free-space, r is the hole radius, and H_0 is the magnetic field of the incident wave. After normalizing the area of the circle to πr^2, Bethe's theory concludes that the transmittance through a subwavelength circular aperture is inversely proportional to the fourth power of the wavelength.

$$T \propto (\frac{r}{\lambda})^4$$

The weaker transmission predicted by Bethe's theory reflects the difficulty of squeezing light through apertures much smaller than its wavelength compared to Kirchoff's theory which predicts higher transmission.

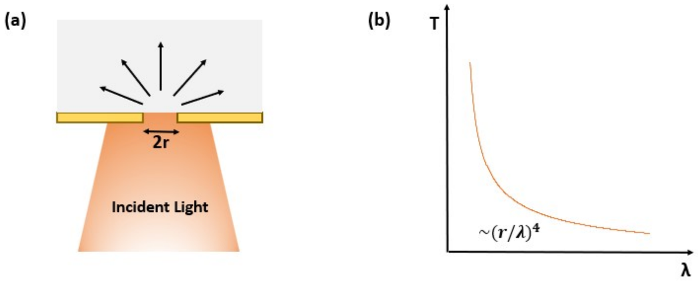

Figure 2.3: The transmission of light through a subwavelength hole. The optical transmission is proportional to the inverse fourth power of wavelength.

Also, If a dielectric medium surrounds the aperture, the wavelength in the medium is scaled as $\lambda = \frac{\lambda_0}{n}$, where n is the refractive index of the medium. Therefore, a larger optical transmission is expected for the same aperture size.

2.4 Extraordinary Optical Transmission

In 1998, Ebbesen and colleagues discovered that when a periodic array of subwavelength holes is patterned onto a metallic film, the transmission through these apertures can be orders of magnitude higher than predicted by Bethe's theory [17]. This phenomenon, known as Extraordinary Optical Transmission (EOT), arises due to the coupling of incident light with surface plasmons—coherent oscillations of free electrons at the metal-dielectric interface. These surface plasmons resonate with the periodic structure of the apertures, creating strong localized electromagnetic fields that facilitate enhanced transmission through the apertures, even though they are much smaller than the wavelength of light [18].

2.5 Surface Plasmons

Surface plasmons (SPs) are a type of electromagnetic wave that occur at the interface between a metal and a dielectric material. We can classify them into two categories: propagating surface plasmon polaritons (SPPs) that travel along a smooth metal-dielectric boundary, and localized surface plasmons (LSPs) that confine to structures like nanoparticles. These waves are purely evanescent, meaning that their electromagnetic fields decay exponentially away from the interface, effectively confining the field to the vicinity of the surface. When light interacts with a subwavelength aperture, and if its frequency matches the resonant frequency of the SP mode, it can induce a strong, localized electromagnetic field around the aperture. Due to the confinement of SPs near the metallic surface, there is a significant enhancement of the electromagnetic field compared to the incident light. Moreover, since the effective wavelength of SPs is shorter than the free-space wavelength of light, they can generate highly localized fields that have prompted extensive research into plasmonic trapping and manipulation techniques [19].

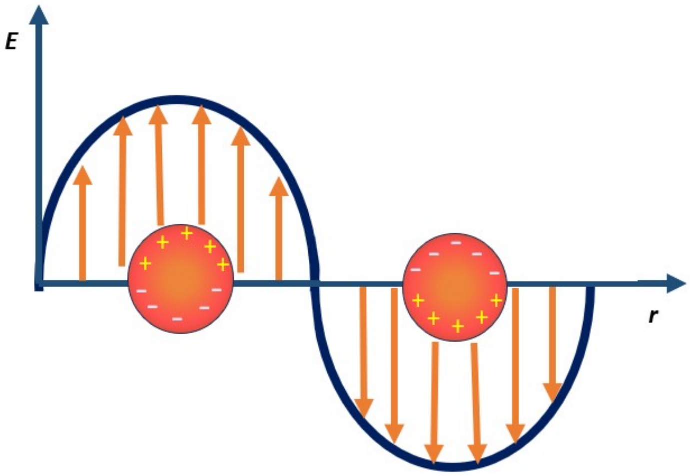

Figure 2.4: Localized surface plasmons as an oscillating system

The resonance frequency of surface plasmons is reliant upon the size, shape, and material composition of the metallic nanoparticle, in addition to the dielectric characteristics of the adjacent medium [20].

2.6 Nano Optical Tweezers

Nano Optical Tweezers enable trapping of particles as small as 10 nm [21] using optical powers considerably lower than that required by conventional tweezers for larger particles. Plasmonic tweezers utilize light's ability to excite plasmons on a metallic surface. Nanostructures are integrated into the trapping surface of plasmonic tweezers to create a sub-wavelength trapping volume. This increases the electric field gradient and, therefore, the strength and efficiency of the trap. Nanostructures like nanoholes, nanopillars, nanopyramids, and nanoapertures [10] are used to enhance plasmon intensity through resonance or the formation of localized hotspots, resulting in electric field intensities 10 to 10^4 times greater than the incident field. In addition, nanoaperture based trapping has the advantage of good thermal conductivity of the metal film which significantly reduces the heating effect [22].

The nanoaperture trap works on the principle of Self induced back action (SIBA), a form of optical tweezing where the trapped particle actively contributes to the trap's stability. It was demonstrated experimentally trapping of a single 50 nm polystyrene sphere using a SIBA optical trap based on the transmission resonance of a nanoaperture in a metal film [23]. Unlike traditional optical tweezers, where the trapping force is directly related to the gradient of the light field intensity, SIBA trapping relies on the interplay between the trapped object and the optical field, creating a feedback loop that enhances the trapping potential.

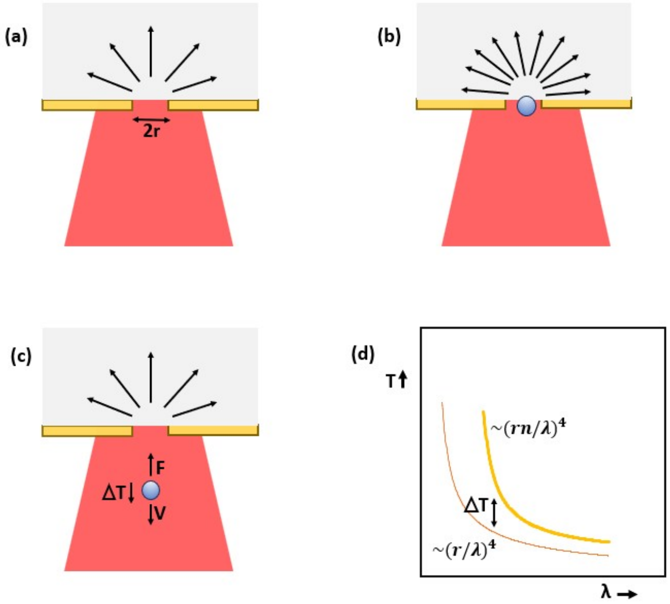

Figure 2.5: Optical transmission through a single subwavelength hole (a)without particle (b)Transmission enhanced with dielectric loaded (c)Transmission decreases as the particle moves away from the trap (d) change in transmission, ΔT with dielectric loading.

As Beth's theory shows, the presence of a small particle in the aperture significantly increases the electric field intensity and thus provides a deeper potential well. The transmission decreases when the particle moves away from the aperture, resulting in a reduced photon momentum flow through the aperture. According to Newton's third law, an opposing force is expected to act on the particle to counterbalance this change in momentum, directing the particle back towards the aperture and restoring equilibrium. Conversely, if the particle moves deeper into the aperture, the transmission increases, and the restoring force pushes the particle outward. Additionally, a lateral force arises due to the asymmetry of the particle's position within the aperture. As the particle approaches the edge, it focuses the electromagnetic field in that region, thereby enhancing the trapping effect [23].

2.7 DNH Optical Tweezers

Several nanoaperture structures have been developed to trap smaller particles. DNH optical tweezers have successfully shown the trapping of 12nm silica spheres [24] and single molecules down to 4kDa [25]. A DNH is a nanostructure that consists of two closely spaced subwavelength holes etched into a thin metallic film, typically separated by a narrow gap.

The DNH structure offers a unique advantage due to its ability to generate a highly concentrated local field in the small region between the two tips (cusps). This localized field greatly enhances the sensitivity of the optical transmission to changes in the local refractive index, as all the transmitted power through the aperture

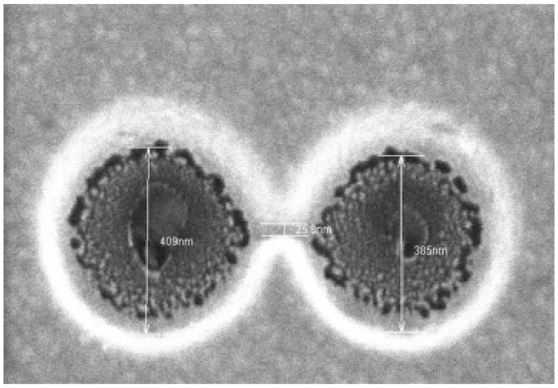

Figure 2.6: Double Nanohole

is focused in this confined area. The change in optical transmission between the trapped and vacant states is directly related to the optical force, as described by Newton's Third Law. Consequently, even a small particle, with dimensions comparable to the strong local field region, can induce a substantial change in transmitted power and generate sufficient self-induced trapping force.

If the tip separation is larger than the optimal size, the local field is not as strong, reducing the trapping efficiency. Conversely, if the tip separation is too small, particles are physically blocked from entering the trapping region. This precise control of particle size selection makes the DNH structure for size sorting applications [26]. The most effective trapping occurs when the particle size matches the entire trapping area, highlighting the critical role of steric hindrance in the DNH trap. This phenomenon is contrary to conventional optical traps, where larger particles typically experience stronger trapping forces [24]. In contrast, a circular nanohole, being isotropic, does not provide such localized field enhancement. As a result, only relatively large particles can induce a significant change in transmitted power to generate adequate trapping force. Thus, the double-nanohole design enables the trapping of much smaller particles compared to circular nanoholes. Furthermore, the DNH outperforms rectangular nanoholes in trapping efficiency. Although rectangular nanoholes can also enhance local fields through surface plasmon coupling between the closely spaced sides [18], the enhanced field is distributed along the hole's sides, leading to weaker trapping along the long axis. In contrast, the DNH focuses the trapping force at a single point between the tips, making it more effective for precise nanoscale trapping.

DNH structures can be easily integrated into existing laser tweezer microscopy systems, the tip of the fiber [27], and microfluidic environment [28]. DNH optical tweezing allows for sophisticated study of protein conformational changes [24], small molecule interactions with proteins, label-free investigation of single DNA-protein interactions [29], and so on.

The DNH's strong field intensity generates a potential well with a harmonic potential around the trap's center due to the conservative nature of optical forces. The stiffness of the trap is mostly calculated using the autocorrelation method in which the brownian induced intensity fluctuations of the transmission signal is used to determine the trap stiffness.

Langevin's equation can be used to model the motion of a particle in an optical trap influenced by thermal fluctuation and drag force given by:

$$m\frac{d^2x(t)}{dt^2} + \gamma v(t) + kx(t) = \zeta(t) \tag{2.12}$$

1. $m\frac{d^2x(t)}{dt^2}$ represents the inertial force acting on the particle due to its acceleration. m is the mass of the particle in the trap and $x(t)$ is the instantaneous position of the particle.

2. $\gamma v(t)$ is the frictional force and is proportional to the velocity of the particle under the Brownian motion.

3.The third term, $kx(t)$ refers to the restoring force on the particle as it tries to escape from the trap. k is the force constant or stiffness of the trap. The values of k are influenced by various factors such as particle size, shape, refractive index, DNH geometry, and laser power. $\zeta(t)$ is a stochastic force term representing thermal fluctuations and background noise due to the fluid on the Brownian particle. In overdamped conditions, where inertia is negligible compared to frictional forces, this term can often be omitted, simplifying the equation to the overdamped Langevin equation:

$$\frac{dx(t)}{dt} = \frac{k}{\gamma}x(t) + (\frac{2K_BT}{\gamma})^2\zeta(t) \tag{2.13}$$

the term $\frac{2K_BT}{\gamma}$ scales the noise term $\zeta(t)$ to ensure that it reflects the correct magnitude of thermal fluctuations at temperature T. It is derived from the fluctuation-dissipation theorem.

The time constant $\tau$is related to trap stiffness by

$$\tau = \frac{\gamma}{k} \propto \frac{\eta r}{\alpha \nabla |E|^2} \tag{2.14}$$

where α is the polarizability of the particle and E is the electric field. The power spectrum of the position of the trapped particle can be derived by applying a Fourier transformation to the Langevin equation[30]. The corner frequency f_c can be calculated from the Lorentzian fit of the power spectral density of the trapped signal. It is given by:

$$f_c = \frac{1}{\tau} = \frac{k}{\gamma} \tag{2.15}$$

Thus f_c gives the stiffness or strength of the trap.

The nanospheres at the DNH aperture experience additional drag force due to wall effects from the nanohole structure.Taking boundary effects into consideration the parallel Stokes' drag coefficient is estimated using Faxén's law as

$$\gamma_{\parallel} = \frac{6\pi\eta r}{[1 - \frac{9}{16}(\frac{r}{h}) + \frac{1}{8}(\frac{r}{h})^3 - \frac{45}{256}(\frac{r}{h})^4 - \frac{1}{16}(\frac{r}{h})^5]} \tag{2.16}$$

Where η is the viscosity, r is the radius of the particle, and h the distance from the nanostructure wall to the center of the particle [31].

One method to size the proteins is the Root Mean Square Deviation (RMSD) method which gives the dependence on the root mean squared fluctuations of the signal with respect to the molecular weight of the protein that is trapped [26]. The potential energy of a Rayleigh particle is given by:

$$U = \frac{1}{2}\alpha|E|^2 \tag{2.17}$$

The potential energy is proportional to the intensity so their RMSD values are proportional as well.

$$\sqrt{\langle U^2 \rangle} \propto \sqrt{\langle I^2 \rangle} \tag{2.18}$$

By plugging Eq(2.18) in (2.19) we get

$$\sqrt{\langle I^2 \rangle} \propto \alpha \sqrt{\langle \frac{|E^4|}{4} \rangle} \tag{2.19}$$

Here we can see that the RMS of transmission signal intensity will scale with polarizability, which scales with particle volume(r^3), resulting in a linear dependence with molecular weight, provided the mass density remains constant. The full width at half maximum (FWHM) of the histogram of the trapped signal also gives the root mean square (RMS) variation of the signal.

Time constant τ can be also used to size the trapped particles. From Eq(2.14),

$$\tau \propto \frac{1}{r^2}$$

In terms of volume,

$$\tau = V^{(-\frac{2}{3})} \tag{2.20}$$

The characteristic time of the autocorrelation of the trapping laser intensity fluctuations follows a scaling relationship that is proportional to the particle's volume raised to the power of -2/3.

2.8 Concluding Remarks

In conclusion, this Chapter has provided a comprehensive overview of the fundamental principles and theoretical framework behind optical tweezers, particularly focusing on the single-beam gradient force trap and its limitations. The advantages of aperture-based optical traps were explored, including their ability to overcome the constraints of conventional optical tweezers. Additionally, the concept of extraordinary transmission, SIBA trapping, and nanoaperture optical trapping focusing on DNHs, that enhance trapping at the nanoscale were discussed. These principles will become useful for understanding how the proposed experiments work in the following section.

Chapter 3

Methods

This chapter explains the methods used in the experiments performed for this thesis. It explains two fabrication methods for DNHs: Colloidal Lithography and Focused Ion Beam Milling. This chapter also gives an overview of the preparation of the trapping solution, sample preparation, and a detailed explanation of the optical tweezer setup.

3.1 Nanofabrication

3.1.1 Colloidal Lithography

Colloidal lithography is a low-cost, simple, bottom-up approach used to fabricate DNHs. Firstly, a 75×25×1 mm glass microscope slide (Fisherbrand) is cut into three pieces using a diamond scribe. These slides are blow dried with compressed nitrogen to remove dust and sonicated in ethanol for 10 minutes. After sonication, they are rinsed with ethanol and acetone, blowdried with compressed nitrogen, and stored in clean plastic Petri dish containers. It is a good practice to visually check if the glass slides are properly clean without any large dust particles. The fabrication process involves determining the appropriate diameter of polystyrene spheres based on the particle to trap. Polystyrene spheres(PS) from the Alpha Nanotech brand were used to fabricate DNHs. PS solution was prepared by mixing 10 μL of suspended PS in 1 mL of ethanol. Gently mix the solution by pipetting it up and down. Spread 10 μL of this PS solution on the clean glass slide in a zig-zag pattern starting from one corner using a micropipette. Allow the slides to dry overnight for the ethanol to evaporate where the PS will form clusters at random. The cluster of interest is a dimer that will result in a DNH aperture once the fabrication procedure is complete. After evaporation, the coated slides are cleaned in a plasma cleaner for 170 seconds using a Harrick PDC plasma cleaner to tune the dimer cusp size. It has been found that etching slides individually and placing them in the machine at the same location each time ensures that the plasma is consistent and provides greater control in tuning the cusp size [32].

Plasma Ethched slides are then sputtered using the AMF's Mantis QUBE system. The samples are securely attached to the mounting plate using a double-sided thermal tape, with the PS coated side facing outwards. The titanium layer, forming an adhesion layer for the gold, is sputtered at a thickness of 7 nm, followed by the gold layer at 70 nm. The gold coated sample slides are then sonicated in ethanol for 7-8 minutes to remove the beads. The samples are rinsed with ethanol and blow dried with nitrogen. If sonication is unsuccessful, a tape lift off procedure is recommended. Dab the tape on your gloved hand to remove most adhesive and gently tap the gold surface to remove the PS. It has been observed that some residues remain inside the holes after the sonication process. This could potentially be remnants of the PS spheres that were not fully removed during sonication or cleaning. One possible explanation is that during fabrication, processes such as etching or sputtering may have caused the polystyrene spheres to partially embed into the substrate. However, this residue does not impact the trapping process or efficiency, as the primary focus is on the gap between the holes, which remains unaffected.

3.1.2 Focused Ion Beam Milling

The focused ion beam (FIB) milling technique is a top-down method for fabricating DNH. This technique uses highly accelerated metal ions, like low-temperature gallium, to sputter material off the surface and mill structures with precise dimensions. To make gold samples for fabrication, the glass slides were cleaned and prepared(as explained above), followed by the deposition of a 7 nm titanium adhesion layer and a 70 nm gold layer using the AMF's Mantis QUBE sputtering system. The DNHs on a gold film were fabricated using the Hitachi FB-2100 system. The desired milling pattern was designed as a bitmap image and input into the FIB control software. The Hitachi FB-2100 system can process bitmaps with a maximum

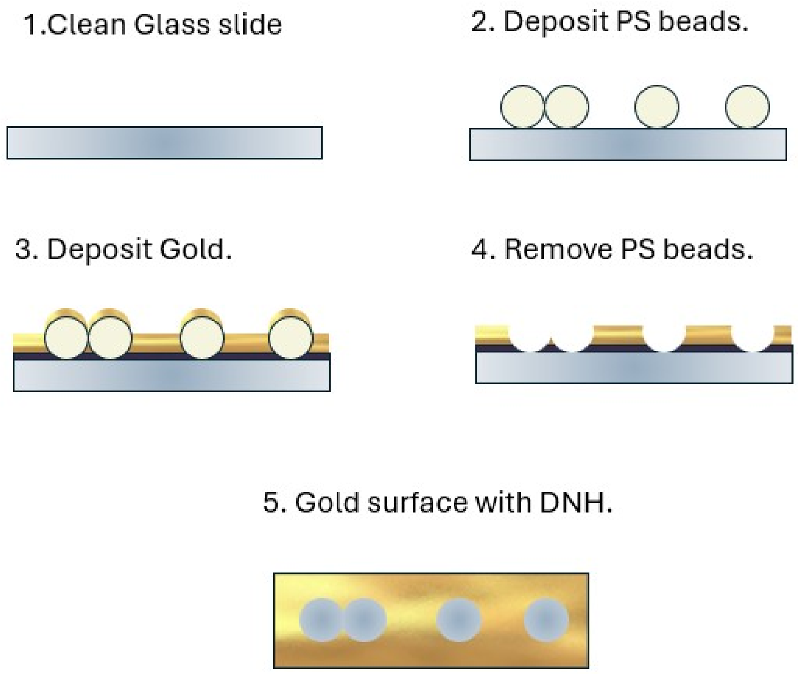

Figure 3.1: Steps in Colloidal Lithography.

resolution of 2000×2000 pixels, corresponding to a physical area of 400×400 $\mu\mathrm{m}^{\mathbf{2}}$ on the sample surface.

The bitmap was created in MATLAB as a 2D matrix where 0s represented exposed regions (black pixels) and 1s represented unexposed regions (white pixels). Figure 3.2 illustrates a sample bitmap used for the DNH fabrication. It consists of two solid circles, with their diameters and separation distance adjusted to control the size and tip separation of the DNH. Due to the finite width of the FIB beam, the center-to-center distance between the circles in the bitmap was set to be approximately 30–40 nm greater than the circle diameter to ensure that the resultant nanoholes would just touch each other. Additionally, a thin line connecting the two circles was included in the design to prevent any residual metal from remaining in the gap between the tips.

The milling process was carried out using an ion accelerating voltage of 40 kV and a beam limiting aperture of 15 μm diameter, under 60k× magnification. Each DNH was milled with 80 passes and a dose time of 5 ms per pass to achieve precise patterning. Large fiduciary markers are fabricated near the DNH structures for ease of identification on the optical tweezer setup.

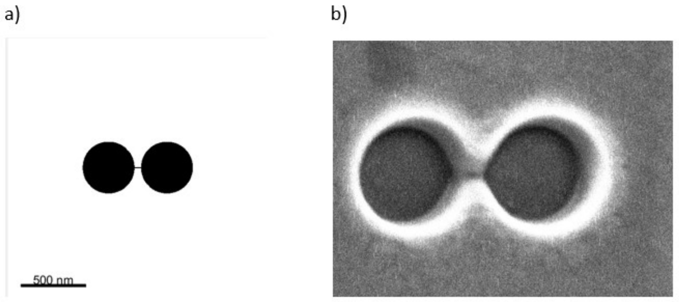

Figure 3.2: (a) Bitmap (b) DNH using FIB.

The FIB technique is more expensive and time-consuming compared to colloidal lithography, which has demonstrated effective trapping results. Regular DNHs were fabricated using colloidal lithography, while FIB was reserved for the fabrication of Asymmetric DNHs, as will be discussed later.

3.2 Characterization of DNHs Using SEM

The fabrication process is characterized by using a Hitachi S-4800 Scanning Electron Microscope (SEM) at the Advanced Microscopy Facility, maintained by CAMTEC at the University of Victoria. Colloidal lithography introduces many different structures on the slide as shown in Figure 3.3. Measurements of the hole diameters and cusp separations are taken to confirm the success of the fabrication. Typical SEM operating parameters for a DNH include a working distance of 4 mm, an accelerating voltage of 2 kV, and a 10 μA electron beam current.

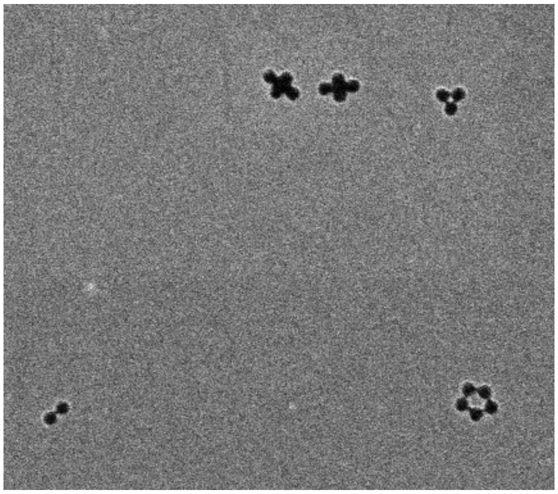

Figure 3.3: SEM image showing different clusters of holes from colloidal lithography

3.3 Trapping Solution and Sample Encapsulation

For polystyrene trapping, 1 μL of ultrapure water is first added to a 1.5 μL Eppendorf tube, followed by 20 μL of the selected polystyrene bead size. The solution is gently mixed by rolling the tube or by gently pipetting the solution up and down to ensure even distribution.

For protein samples, Bovine Serum Albumin (BSA), Carbonic Anhydrase (CA), and Cytochrome C (CTC) are obtained from a Sigma-Aldrich size-standard kit (MWGF200-1KT). These proteins are prepared at a concentration of 0.1 wt/v % by weighing them in 1.5 μL Eppendorf tubes and kept in 20 μL aliquots at -20°C. Phosphate-buffered saline (PBS) is used as the solvent in the protein experiments.

To prepare the gold sample for trapping, a 24×60 mm, 1.5 mm thickness coverslip (Fisherbrand 22266882) is thoroughly rinsed with isopropyl alcohol, acetone, and ethanol. After cleaning, the coverslip is blow-dried using nitrogen gas and carefully placed on fresh lens paper. An image spacer (Grace Bio-Labs GBL-654008-100EA) is adhered to the coverslip, and 10 μL of the trapping solution is then pipetted into the spacer. The DNH sample is positioned on top of the spacer, ensuring the gold surface comes into direct contact with the solution.

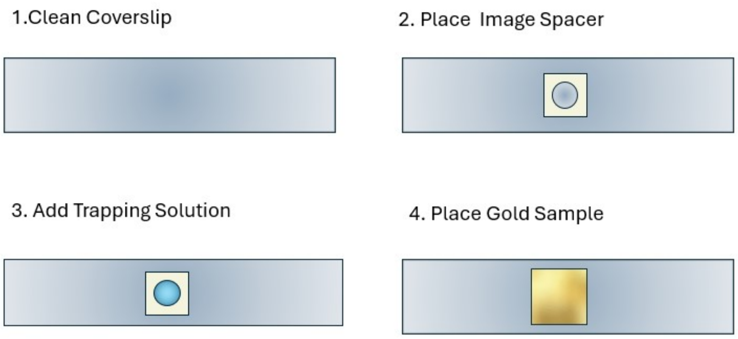

Figure 3.4: Procedure for Preparing a Trapping Sample

3.4 Optical Tweezer Setup

The optical trapping setup employs a fiber-coupled, collimated 980 nm laser (JDS Uniphase 27-7602-200-TE, solid state) for trapping. A half-wave plate and linear polarizer are positioned in the beam path to control the polarization and orientation of the light, crucial for distinguishing between a double or single nanohole. The laser beam is then expanded and collimated using two lenses, which increase the beam's spot size from approximately 2 mm to 4 mm, before it is directed onto a dichroic mirror and enters the microscope column.

A 100× oil-immersion objective tightly focuses the beam onto the DNH sample, while transmission light passing through the DNH is collected using a 10x condenser microscope objective (0.25 numerical aperture), and the reflected beam follows the excitation laser path. A white light LED emits light through the top of the column, passing through the 10x objective, the sample, and the 100x objective before reaching the dichroic mirror. A lens focuses this light onto a charge-coupled device (CCD) camera. However, the reflected laser beam is intense enough to overpower the LED signal by passing through the dichroic mirror and reaching the CCD.

The transmitted signal is directed to an avalanche photodiode (APD) through another dichroic mirror and a focusing lens, where the trapping signal is detected. The sample is mounted between the oil-immersion objective and the condenser microscope objective and aligned using a piezoelectric-controlled XYZ sample stage, providing 20 nm positioning precision. The sample is positioned with the glass cover slide facing the oil-immersion objective, while the chip is placed on the XYZ sample stage with the gold side facing downward. This arrangement allows the gravitational force to pull the nanospheres away from the gold film, while the optical force works against gravity. A drop of immersion oil (refractive index of 1.51) is applied to the glass cover slide below the micro-well. Excess oil can cause the sample to slip, compromising precise positioning and leading to undesired measurement variations. It is essential to clean the oil-immersion objective with a lens wipe before and after each use to avoid residual oil affecting subsequent measurements. On the CCD camera, the DNH appears as bright oval-shaped structures.

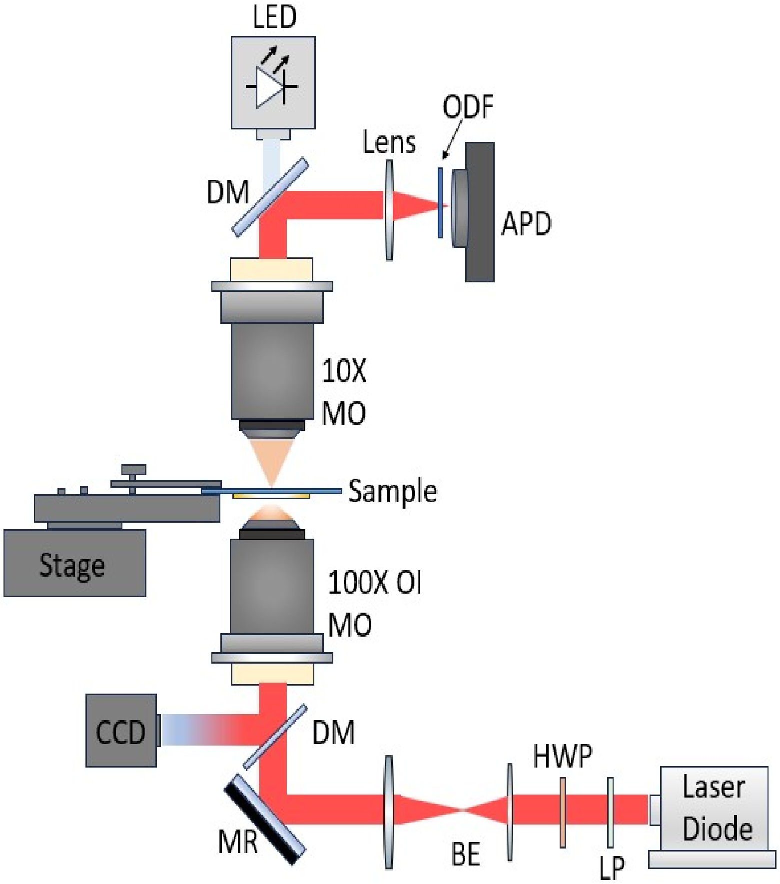

Figure 3.5: Schematic of optical setup: LP: Linear Polarizer, HWP: Half Wave Plate, BE: Beam expander, MR: Mirror, DM: Dichroic Mirror, CCD: Charge Coupled Device, OI MO: Oil Immersion Microscope, ODF: Optical Density Filter, APD: Avalanche Photodiode.

The DNH, being asymmetric, can be further distinguished by rotating the half-wave plate and observing changes in transmission. As the linearly polarized light is rotated from the short axis to the long axis of the DNH, a significant change in transmission is observed

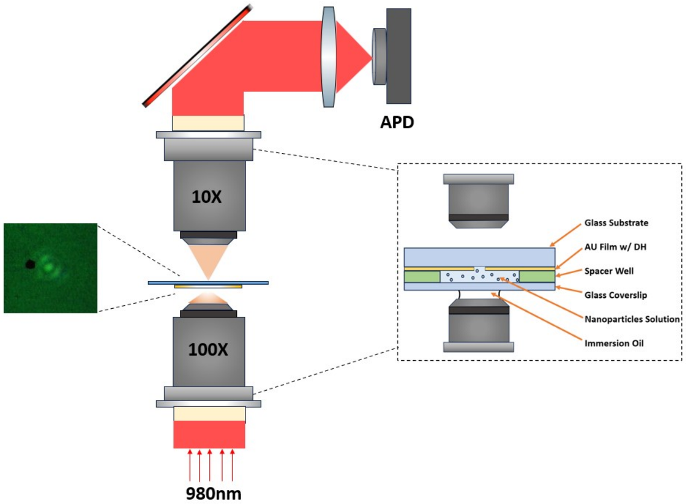

Figure 3.6: Optical Tweezer setup with Sample and DNH as seen through CCD camera.

due to its asymmetry. Data collection involves converting the analog optical transmission signal measured by the APD into a digital signal using an Omega USB-4711A Portable Data Acquisition Module. Data analysis is carried out using Python.

3.5 Concluding Remarks

This chapter gave an overview of the fabrication methods for DNHs, preparation of the trapping solution, sample preparation, and also a detailed explanation of the optical tweezer setup.

Chapter 4

Study of Protein Conformational Dynamics and Electrostatic Interactions using DNH Optical Tweezers.

This chapter has two parts: The first part deals with the label-free study of BSA Conformational Dynamics using DNH optical tweezers where it studies the Gibbs energy between the different conformational states of BSA using free energy diagram. This published work is first authored by my colleague Matthew Peters. The author contributed to the work by providing trapping events at different power levels for the experiments. The second part is the study of the effect of electrostatic interactions between proteins with different charges and the gold surface on the trapping stiffness.

4.1 Label-Free Study of BSA Conformational Dynamics

4.1.1 Introduction

Bovine serum albumin (BSA) is a globular protein with a molecular weight of 66.4 KDa and a hydrodynamic radius of 5.45 nm. BSA is composed of 583 amino acid residues; it is a single, nonglycosylated protein. BSA self-associates to form dimers and higher oligomers and is known to bind ligands, which in many cases induce a conformational change in the protein [33]. BSA is the predominant protein in blood plasma, constituting approximately 60% of total protein and 80% of colloid osmotic pressure; it possesses significant properties in the transport and deposition of several endogenous and exogenous chemicals in the bloodstream [34]. Since BSA has significant structural and functional similarities to human serum albumin (HSA), it is often used as a proxy for studying human albumin because it behaves similarly in solution and is easier to obtain.

The dynamics and interactions of proteins often require to modify the protein with fluorescent labels and/or tethers. Studies have shown that these modifications often alter the protein's biophysical properties and limit the observation time due to quenching. This is because the solution behavior of a protein is very sensitive to changes in its environment [35]. Tethering uses some of the available binding sites for surface attachment and restricts the free motion of the protein and hence prevents monitoring binding partners in their native state. Vibrational energy can induce structural transitions in biomolecules, altering their effective size, shape, or polarizability, which in turn can impact the trapping efficiency and stiffness in optical tweezers. Vibrational modes refer to the quantized oscillations of atoms within a molecule, encompassing movements such as stretching, bending, and twisting of chemical bonds. Proteins and other biomolecules exhibit unique vibrational modes that are specific to their structure and composition. When molecules like proteins are trapped optically, their internal vibrational modes play a role in how they interact with the trapping field. This interaction can influence the overall behavior and dynamics of the trapped biomolecule, impacting the effectiveness of the trapping process. Nanoaperture optical tweezers are an interesting method for studying real-time interactions at the single-molecule level in a label-free, free-solution environment. We use DNHs, which is well explained in Chapter 1 for trapping. 980nm wavelength laser was used to trap the proteins and data was analyzed using Python.

4.1.2 Conformational Changes in Unlabelled and Labeled BSA

Conformational changes in BSA are subjected to environmental conditions such as pH, temperature, ionic strength, and the presence of ligands [36] [37]. The N or the Native state is the normal, stable conformation of BSA at neutral pH (around 7) and room temperature. In this state, BSA maintains its compact, globular structure. The protein has three domains (I, II, III) which are stabilized by an internal network of disulfide bonds, each bearing many ionizable groups with opposite signs [38]. At pH 3.5, BSA transitions to the F or fast state. In this state, the protein undergoes a partial unfolding, resulting in increased flexibility. BSA unfolds into the most expanded state, also known as E state. This state is characterized by significant structural unfolding, exposing more of its hydrophobic regions and reducing its binding specificity [39].

DNH optical tweezers are used to see the conformational changes of BSA and labeled BSA, seen by changes in the optical transmission of the trapping laser beam through the nanoaperture, where transitions from the normal to fast form of the protein increased transmission. The change in transmissions is because the conformational changes of a protein alter the structure, and thus its polarizability [40]. The local temperature of the protein was varied by changing the trapping laser power. The power was measured using a Thorlabs laser power meter, positioned after the microscope objective. Previous studies show the temperature increase due to heating from an incident laser [41] [42]. Figure 4.1 shows the temperature dependence with laser power.

Here, fluorescein isothiocyanate (FITC) labeled BSA and unlabelled

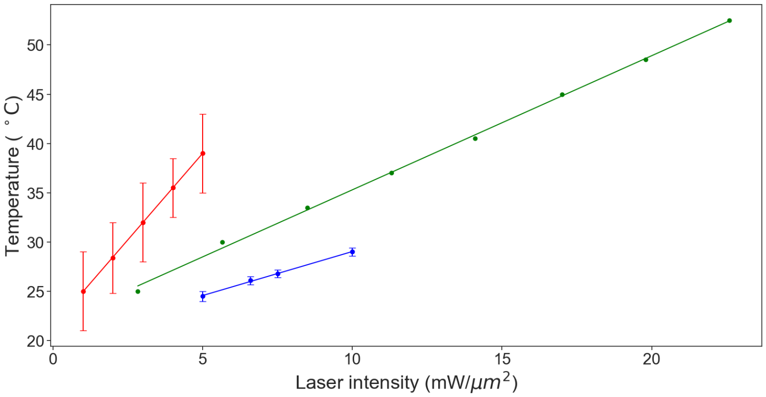

Figure 4.1: Temperature dependence with laser power. Data from [42] [43] [44].

BSA were used to take measurements. FITC binds to site II of BSA, filling an empty hydrophobic site of domain III, noting the FITC itself is also hydrophobic [45]. FITC binding to BSA changes the molecular weight from 66.4 to 71.1 kDa [46]. While the RMS value of the trapped signal generally shows a linear relationship with molecular weight, the RMS value for FITC-labeled BSA is lower than that of unlabeled BSA. This deviation could be attributed to several factors, such as changes in the protein's structure, or altered interactions with the trapping field caused by the FITC labeling.

Figure 4.2 shows the transmission through DNH for the FITC-labeled BSA and the unlabeled BSA. Conformational changes in a single BSA protein are easily identified as changes in transmission through DNH. A k-Means state recognition algorithm was used to find the experimental state switching. The protein is initially

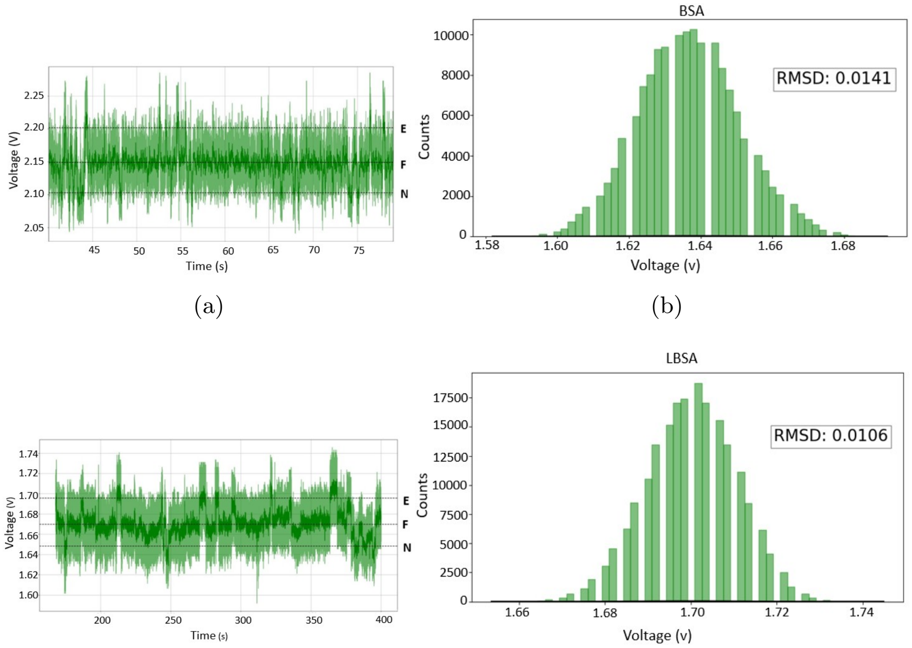

(a) (b)

(c) (d)

Figure 4.2: (a) Unlabelled BSA conformation states (b) Histogram distribution of the trapped Unlabelled BSA (c) FITC Labeled BSA conformation states (d) Histogram distribution of the trapped FITC Labeled BSA.

trapped in the N-state and quickly transitions to the F-state and rarely to the E-state. The RMSD of the trapped data provides a measure of the spread or variability of the data points around their mean value. A lower RMSD value suggests that the particle is held tightly in the optical trap, with minimal movement. The histogram of a trapped signal provides valuable insights into the probability distribution of the signal's amplitude or voltage over time. For a stable trap, you might see a Gaussian (normal) distribution, where the signal is centered around a mean value, with most voltage readings close to the mean and fewer readings at the extremes. If the histogram shows multiple peaks, the particle is switching between different trapped states.

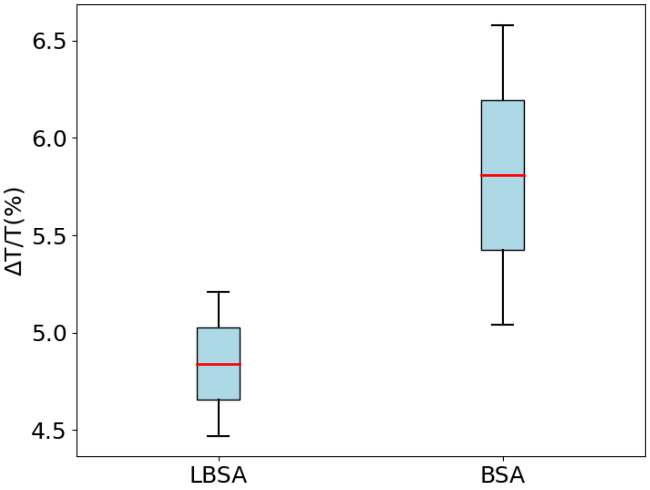

Figure 4.3: Transmission through DNH measured for unlabelled BSA and labeled BSA.

Figure 4.3 shows the change in the percentage of transmission through the DNH for FITC labeled BSA and unlabeled BSA. The values suggest that the transmission for both labeled and unlabeled BSA are almost the same.

Significant studies were conducted on the trapped data from both labeled and unlabeled BSA by my colleague, Matthew Peters. The energy landscape for the conformational changes of BSA was derived from the probability density function (PDF), which is a binned histogram of the APD voltage recorded over an extended time window. Fluctuations in the transmission signal were associated with both conformational changes of the protein and other movements, such as translational or rotational motion. These fluctuations, along with noise, produce a point spread function (PSF) in the signal that needs to be deconvolved to reveal the true PDF associated with the conformational changes. The PSF for the BSA measurements was estimated to have a standard deviation of 13.4 mV, obtained from the dimer because of its enhanced conformational stability, allowing for longer observation without transitions. The PDF of the raw transmission data was then deconvolved with the Gaussian PSF to obtain the true PDF $P(V)$ which was used to uncover the energy landscape$U(V)$.

$$U(V) = -K_B T ln(P(V)) \tag{4.1}$$

where K_B is the Boltzmann constant and T is the temperature. Figure 4.4 shows the summarisation of all the steps mentioned above. Figure 4.4 (a) shows the trapped signal for different temperatures for unlabeled BSA. (b) shows the visualization of different states of BSA. It gets trapped at the N state, transitions to the F state, and moves to the E state at a higher temperature. (c) shows the energy landscape and probability density function after deconvolution for unlabeled BSA at 314K. The x-axis shows the transmission voltage, which is related to how light passes through the system. The y-axis shows the PDF of BSA's distribution (yellow line) and the free energy is represented in units of $2.5K_BT$, indicating how the energy landscape varies with the transmission voltage (brown line), and (d) shows the linear relation between temperature and change in Gibbs free energy for labeled and unlabeled BSA.

This extracted energy landscape provided equilibrium constants and Gibbs free energy values. Figure 4.5 shows an example of the calculation of change in Gibbs free energy from the energy landscape. ΔG_{FE} is the change in Gibbs free energy of the FE transition.

$$K_{eq} = e^{\frac{\Delta G}{RT}} \tag{4.2}$$

where ΔG is the change in Gibbs energy and R is the gas constant. The change in Gibbs free energy ΔG is related to the enthalpy ΔH

and entropy ΔS of the protein:

$$\Delta G = \Delta H - T\Delta S \tag{4.3}$$

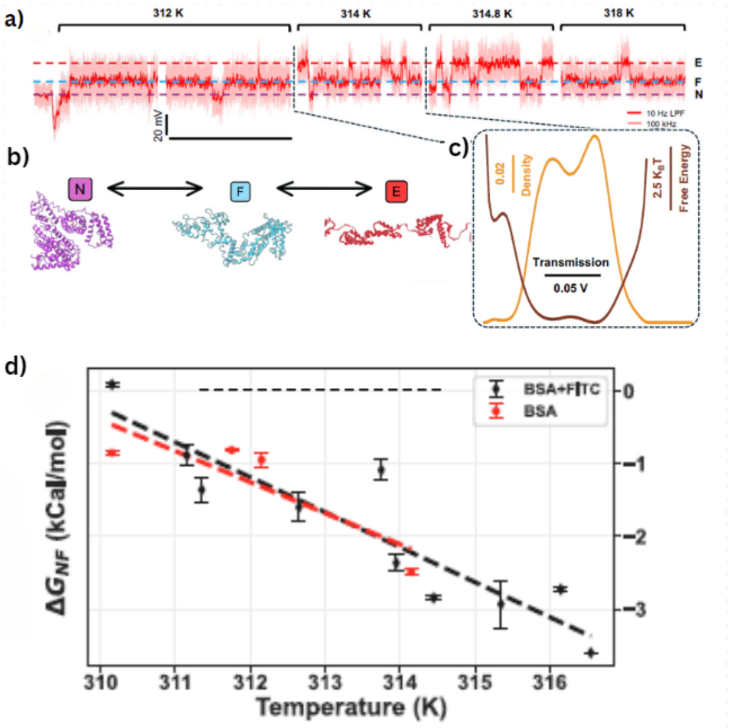

Figure 4.4: (a)Transmission through the DNH measured at different temperatures for unlabelled BSA. Dark red indicates data filtered with a 10 Hz low-pass filter, light red is raw data at 100 kHz.(b)Reaction mechanism diagram for the forward and reverse conformational changes of N ↔ F and F ↔ E. Proteins visualized using PDB: 3V03 for the N-state and PDB: "F isoform of BSA at pH 3.549" for the F-state.No 3D structure is available for the E-state, illustration is traced past work.(c) Energy landscape and probability density function after deconvolution for unlabelled BSA at 314 K.(d) Change in Gibbs free energy for unlabelled and labeled BSA, obtained from the energy landscape at different temperatures. Figures from [47]

.

The entropy, S is expected to remain constant, while the entropic

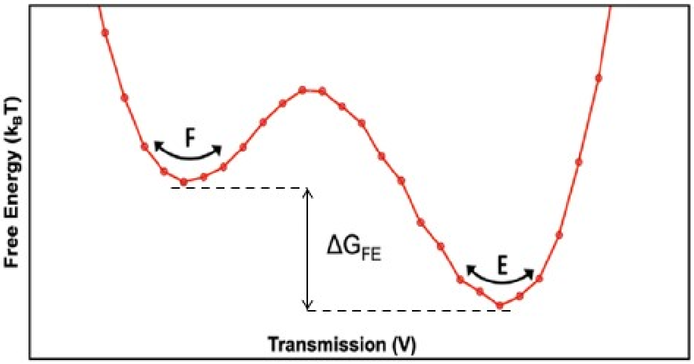

Figure 4.5: Example for the calculation of change in Gibbs free energy from the energy landscape. ΔG_{FE} is the change in Gibbs free energy of the FE transition. Figure adapted from [47]

contribution $T\Delta S$ varies linearly with temperature. For unlabelled BSA, the study found $\Delta G = 130 \pm 55 - 0.43T \pm 0.18$ kcal/mol, and for FITC-labeled BSA, $\Delta G = 150 \pm 20 - 0.48T \pm 0.07$ kcal/mol. The slightly larger values for the FITC-labeled BSA indicate a small impact of the labeling on the results [47]. The author contributed by providing trapping events at different power levels for the experiments.

The conformational dynamics of Bovine Serum Albumin (BSA) showed significant differences between the monomeric and dimeric forms of the protein. This special case arises where a monomeric BSA was first trapped and a second monomeric BSA entered the trap, forming a dimer. The monomeric BSA exhibited a total of three distinct structural conformations, N,F and E states. In contrast, the dimeric form of BSA displayed a reduced range of conformational states, with only two distinct states identified. The two states observed in the dimeric BSA are characterized as the ”closed” (C) and ”open” (O) conformations. This is shown in Figure 4.6. A localized connection in the BSA dimer is established by an intermolecular disulfide bond or a direct structural interaction between the BSA monomers, functioning as a molecular hinge [48].

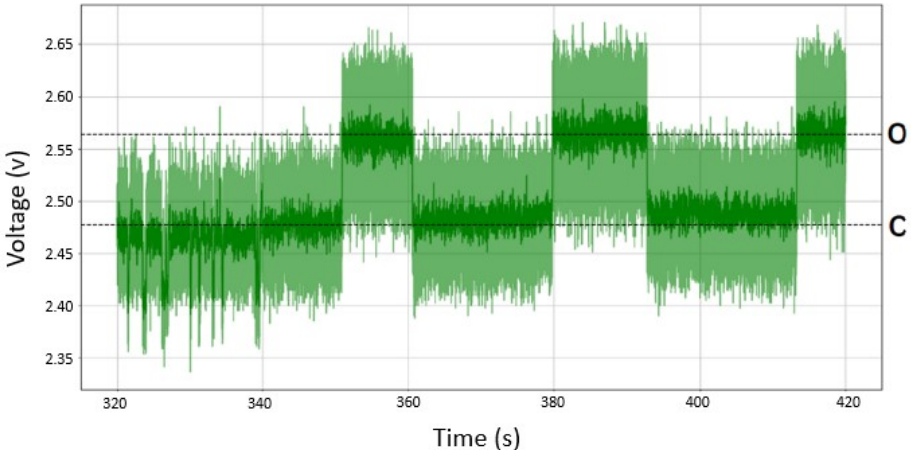

Figure 4.6: Transmission through the DNH showing the initial trap of a monomer and subsequent second trap forming a dimer two-state system.

4.2 Electrostatic Interactions between Proteins and Gold Surface

4.2.1 Introduction

Another study included analyzing the corner frequency of different proteins at different powers. Proteins such as CTC, BSA, and CA were studied for this. CTC is a crucial protein in cell life and death decisions, playing a vital role in electron transfer as part of the mitochondrial electron transport chain (ETC), thereby enhancing energy production. It is highly positively charged with an isoelectric point (pI)of 9.6 [49]. The pI of a molecule is the pH at which the molecule carries no net electric charge. For proteins, the pI is determined by the specific balance of acidic and basic amino acids within the protein. At a pH lower than the pI, the protein tends to have a net positive charge because it gains protons. At a pH higher than the pI, the protein tends to have a net negative charge because it loses protons. CA is a vital enzyme that supports physiological processes related to gas exchange, pH balance, and fluid regulation. The pI of CA is 5.5 [50]. BSA has a low isoelectric point of 5.4 [51]. The proteins were diluted with PBS with a neutral pH for the experiment.

4.2.2 Experiment

Corner frequencies for each of these proteins were calculated at different powers and were plotted against power. Corner frequency is related to laser power through trap stiffness. Corner frequency represents the response time of the particle in the trap, and it's directly related to the trap stiffness k and inversely to the drag coefficient γ. The relationship is

$$f_c = \frac{k}{\gamma}$$

The stiffness of the optical trap increases with the laser power. This is because the optical force, which is responsible for holding the particle in place, increases with the intensity of the laser. Since the laser power determines the intensity, increasing the laser power increases the trap stiffness. The trap stiffness k is typically linearly proportional to the laser power P.

$$k \propto P \tag{4.4}$$

Given that the corner frequency f_c is directly proportional to the trap stiffness k and k is proportional to the laser power, the corner frequency is also proportional to the laser power:

$$f_c \propto k \propto P \tag{4.5}$$

Since the relation between f_c and P is linear, we expect the line to pass through the origin. However, this was not the result obtained with the experimental data. The corner frequencies at varying power were plotted and the linear fit to the frequencies gave positive or negative y-intercept for different proteins. The y-intercept represents the corner frequency when the laser power is zero. A non-zero intercept indicates some trapping effect even without laser input. This could be due to the electrostatic interactions between the proteins and the gold surface. Also, it was noted that the y-intercept being positive or negative depends on the charge the protein carries.

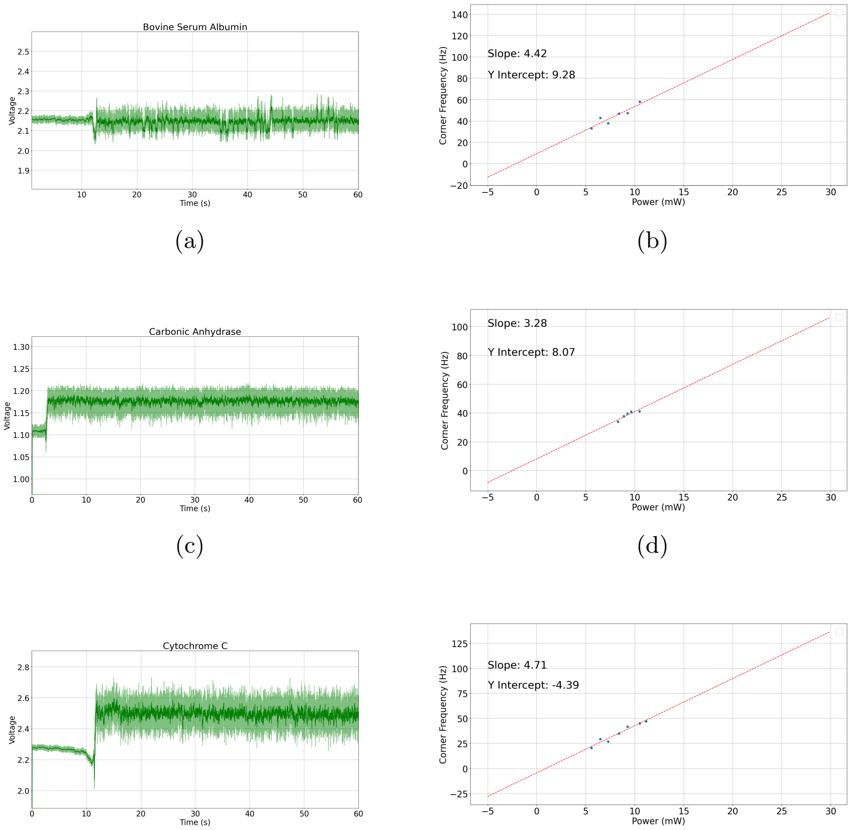

(a) (b)

(c) (d)

(e) (f)

Figure 4.7: (a) Trapping event of BSA (b) Corner frequency vs Laser power for BSA (c) Trapping event of CA (d) Corner frequency vs Laser power for CA (e) Trapping event of CTC (f) Corner frequency vs Laser power for CTC.

The trapping events of different proteins in an optical trapping experiment are analyzed using a plot of corner frequency vs power as shown in Figure 4.7. For BSA and CA, it can be seen that the y-intercept is positive and for CTC has a negative y-intercept. One possible explanation for this would be the electrostatic interactions between the protein and the gold surface. We proceed with the assumption that, in PBS solution, the gold surface generally attains a negative charge due to the adsorption of ions from the buffer and the surrounding environment. BSA and CA have negative charge when diluted in PBS, as their pI is below the pH of the PBS buffer (7.4). Since the gold surface in PBS is also negatively charged, there may be repulsive electrostatic interactions between the protein and the gold surface. These repulsive forces could help stabilize the trapping stiffness at lower laser powers, maintaining a positive corner frequency. The positive y-intercept could indicate that the protein is trapped with some initial stability, even at very low or zero laser power, possibly due to these repulsive interactions. CTC, on the other hand, is positively charged in PBS, which means it may experience attractive electrostatic interactions with the negatively charged gold surface. These attractive interactions could reduce the trap stiffness at low laser powers, leading to a negative y-intercept in your plot. In an optical trap, particles are held in place by the gradient forces from the laser, which pull the particle toward the center of the trap (the region of highest light intensity). This is balanced by scattering and other forces to form a stable trapping potential. If there are attractive forces between the trapped particle and the gold surface, these forces will pull the particle toward the surface, away from the center of the optical trap. The attraction between CTC and the gold surface could make it harder to trap the protein initially, requiring a certain threshold of power to establish effective trapping, which would result in a negative corner frequency extrapolated to zero power. In summary, the interplay between the charge of the protein and the charge of the gold surface seems to influence the trapping behavior. Proteins that experience repulsion (BSA and CA) show positive y-intercepts, while those that experience attraction (CTC) show a negative y-intercept. This suggests that the electrostatic forces at play have a significant impact on the corner frequency behavior in optical trapping experiments.

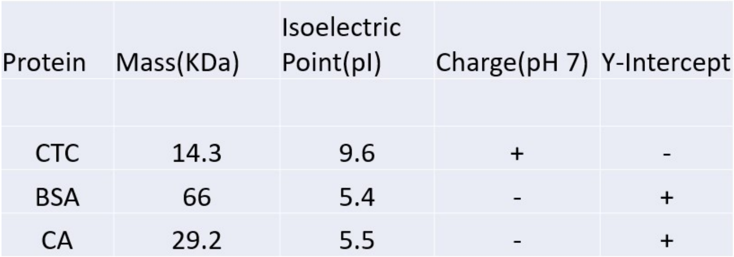

Protein	Mass(KDa)	Isoelectric Point(pI)	Charge(pH 7)	Y-Intercept
CTC	14.3	9.6	+	-
BSA	66	5.4	-	+
CA	29.2	5.5	-	+

Table 4.1: Properties of proteins used in the Experiment

This can be also explained with a capacitor model. In a parallel-plate capacitor, charge accumulates on two conductive plates separated by a distance, with a dielectric (an insulating material) in between. The stored energy, electric field, and capacitance depend on the separation between the plates and the dielectric properties of the medium. The negatively charged gold surface can be viewed as one plate of a capacitor and the protein forms the other plate.

BSA and CA are negatively charged in PBS (like the gold surface), whereas CTC is positively charged. PBS solution acts as the dielectric medium between the gold surface and the protein. The ions in PBS screen some of the electrostatic forces, reducing their effect but not eliminating them completely. In a capacitor, the force between two charged plates is proportional to the charge density and inversely proportional to the square of the distance between the plates. Coulomb's law is used to represent this force:

$$F = \frac{1}{4\pi\epsilon_0}\frac{q_1 q_2}{r^2} \tag{4.6}$$

where F is the electrostatic force between charges, q_1, q_2 are the charges (protein and gold surface), r is the distance between them and ϵ_0 is the permittivity of free space.

For BSA and CA, both the gold surface and the protein are negatively charged, so q_1 and q_2 have the same sign. This results in a positive force, indicating repulsion. As the laser power increases, the trapping forces from the optical tweezers start to dominate, pulling the particle into the center of the trap. The repulsive electrostatic force between the protein and the gold surface prevents the protein from getting too close to the gold surface, stabilizing the trap and maintaining a positive corner frequency. For CTC, which is positively charged, q_1 and q_2 have opposite signs, leading to an attractive force. The force is negative, indicating attraction. The gold surface

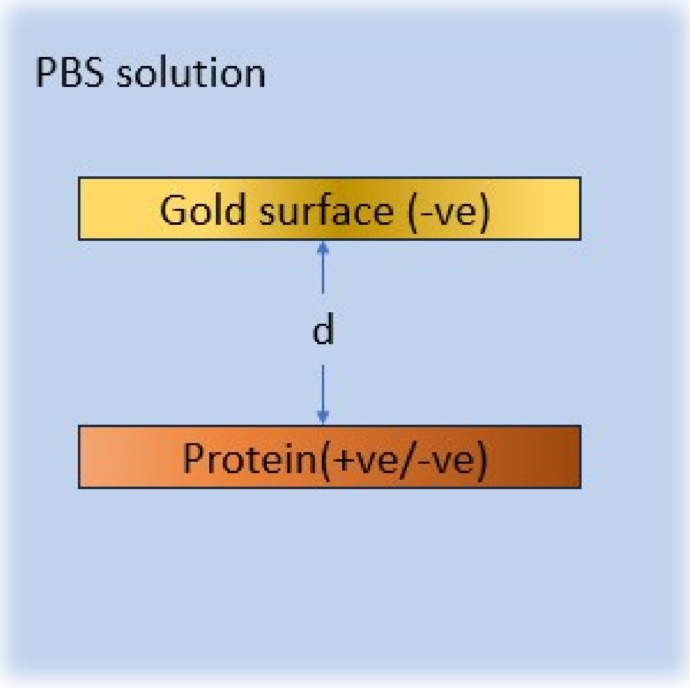

Figure 4.8: A pictorial representation of capacitor model.

pulls CTC toward it, away from the center of the optical trap. This weakens the trap's ability to hold the particle, leading to the negative corner frequency at low power. For a capacitor,

$$C = \epsilon \frac{A}{d} \tag{4.7}$$

where C is the capacitance, ϵ is the permittivity of the dielectric medium, A is the effective surface area of interaction between the protein and the gold surface and d is the distance between the protein and the gold surface. Potential Energy, U is given by:

$$U = \frac{1}{2}CV^2 \tag{4.8}$$

V is the electrostatic potential difference. As the protein moves farther away from the gold surface (i.e., as d increases), the capacitance C decreases because the charges are farther apart. V (related to the charge difference between the protein and the gold surface) stays relatively constant since both charges are negative in PBS. Therefore,U decreases. When the potential energy decreases, the repulsion between the protein and the gold surface weakens. This allows the optical gradient force to dominate and hold the particle in the trap. The opposite happens when d decreases, for CTC.

The magnitude of the protein's charge might also affect the strength of the electrostatic interactions. A protein with a higher net charge might experience stronger electrostatic forces, potentially altering the slope or intercept of the linear fit. For instance, a highly charged protein could exhibit a larger deviation from zero intercept due to more pronounced interactions. However, more study is required for a conclusive conclusion.

Studying polystyrene beads at different salt concentrations (Nacl, Kcl) could provide a more controlled and systematic way to understand the electrostatic interactions in an optical trap. Unlike proteins with complex folding or functional groups, polystyrene beads being simple latex beads makes them an ideal control particle to isolate the electrostatic effects of salt concentration. By increasing the salt concentration, you can effectively screen the electrostatic interactions between the polystyrene beads and the gold surface. This is because when you increase the salt concentration, the added ions screen or shield the charges on the particles and surfaces. This is known as Debye screening. As a result, electrostatic interactions become weaker and the charged surfaces interact less strongly with each other. The changes in salt concentration will modulate the strength and range of these interactions. This helps to observe how trap stiffness and corner frequency change when repulsive or attractive forces are reduced due to higher ionic strength.

4.3 Concluding Remarks

This chapter explored the conformational dynamics of individual, unaltered BSA molecules utilizing DNH tweezers. Gibbs energy for the N to F states was calculated for both labeled and Unlabelled BSA from the free energy diagram and the values show a small effect of labeling on BSA. This Chapter also explored the effect of electrostatic interactions between the gold surface and proteins with different charges on the trapping process. The study was conducted on three proteins: BSA, CA, and CTC.

Chapter 5

Asymmetric DNHs: A Experimental Study

5.1 Introduction

Conventional optical tweezers require a strong light intensity gradient and hence cannot be used on particles smaller than the diffraction limit of light(∼250nm) [52]. However, plasmonic tweezers overcome these limitations by exploiting SPR, which occur when light interacts with metallic nanostructures. These structures generate highly localized and intense electromagnetic fields, allowing for the trapping of nanoscale particles with much lower light intensities. The strong field confinement enables plasmonic tweezers to trap particles as small as a few nanometers, significantly beyond the diffraction limit of light [53]. As a result, plasmonic tweezers are more effective for trapping nanoparticles, biomolecules, and other sub-wavelength objects, making them ideal for applications in single-molecule studies [54] [29] [55]. They are also suitable for applications in optical communications, nanoelectronics, sensing, and optical imaging because of their strong optical gradient energy confinement. Various nanostructures such as nanorods, nanoapertures, nanodisks, and bowtie antennas enhance trapping stiffness by generating localized SPR [10]. Among these, DNH structures play a significant role in enhanced second harmonic generation, surface-enhanced raman scattering (SERS), and fluorescence enhancement. The narrow gap between the two symmetric holes leads to local field enhancement resulting in a strong trapping point [56].

In this chapter, a new nanostructure, ADNHs are experimentally explored, to study its trapping efficiency and control in plasmonic optical tweezers. Here, two nanoholes of different sizes are separated by a very small distance in gold. In other words, there is no gap between the two holes. The main intention of this structure is to explore the possibility of dark mode to optimize various aspects of optical manipulation. The bright mode and dark mode refer to different types of plasmonic resonances that affect how the nanostructure interacts with light. Dark modes can be used to boost the trapping efficiency and bright modes can be used to improve light-matter interactions, which is essential for sensing [57].

5.2 Theory

ADNHs are alterations of the symmetric DNH structure used in plasmonic trapping. It is comprised of two nanoholes of varying diameters that are separated by a small distance and are fabricated on a gold film. These ADNHs induce unique plasmonic effects that can be used to improve the optical trapping, sensing, and manipulation of nanoscale particles. In addition, the gold layer in between the holes also helps in field enhancement near the edges of the nanoholes. In contrast to symmetric DNHs, the two nanoholes' differing sizes or geometries produce asymmetric field distributions and unique plasmonic resonances. The disparity in hole sizes or shapes in ADNHs results in each nanohole resonating at a distinct frequency. The geometric parameters and the surrounding material determine the resonance frequency ω of each nanohole. We can anticipate that each nanohole will produce localized fields of varying magnitudes at the same incident light frequency ω if we designate the resonance frequency for two nanoholes of varying sizes as $\omega 1$ and $\omega 2$. For ADNHs, since $\omega 1 \neq \omega 2$, the fields generated by each hole are not in phase, it results in constructive or destructive interference that generates asymmetric plasmonic field enhancements around each hole, which can in turn result in more localized and stronger "hot spots" in specific regions of the nanostructure. These hotspots are often off-center or non-uniform. This has the potential to increase the efficiency of ADNHs in trapping particles with asymmetric shapes or varying dielectric properties, by enhancing entrapment in specific regions and decreasing it in others. However, asymmetric plasmonic field enhancements lead to unequal trapping forces, where one nanohole may confine particles more effectively than the other. Nevertheless, this asymmetric trapping can occasionally be advantageous for optimizing the plasmonic response to specific light wavelengths or for trapping a broader spectrum of particle sizes. In addition, the asymmetry in the nanohole size causes variations in the resonant frequencies of the localized plasmons. The gold between the holes ensures the plasmons remain confined, resulting in strong gradient forces that enhance trapping. The dark-field mode arises when radiation from one nanohole destructively interferes with that from the other, as they are entirely out of phase, leading to low radiation efficiency. When a dielectric particle enters and dielectrically loads one of the nanoholes, this destructive interference in the far field is altered, restoring the transmission light intensity. The resulting change in transmission intensity, caused by the incoming nanoparticle, leads to a corresponding change in photon momentum. According to Newton's third law, this momentum change exerts a reactive force on the particle, generating an intense optical trapping force. This non-radiative mode is critical for optical trapping. The bright-field mode is a radiative plasmonic resonance characterized by strong coupling to the far field, resulting in efficient scattering and radiation of light. In plasmonic nanostructures, the bright mode arises when plasmonic oscillations are in phase, leading to increased excitation and emission of photons. Bright-field modes are particularly useful in applications requiring strong optical signals, such as photoluminescence enhancement, fluorescence imaging, and optical sensing. While using two different laser wavelengths is a common approach to excite both bright and dark modes independently[57], in some cases, if the bright and dark modes have overlapping or closely spaced resonances, a single wavelength could excite both modes simultaneously. In this study, however, the possibility of increasing trapping efficiency by exciting dark mode is explored.

5.3 FDTD Simulation

Figure 5.1 presents the results of an FDTD simulation conducted to analyze the electric field distribution in ADNHs, providing better understanding into the optical forces acting within the nanoholes. For comparison, the electric field distribution of a symmetric DNH was also simulated using the same method, allowing for a side-by-side evaluation of how symmetry affects the field.

The plasmonic scattering from the Regular DNH is polarization-

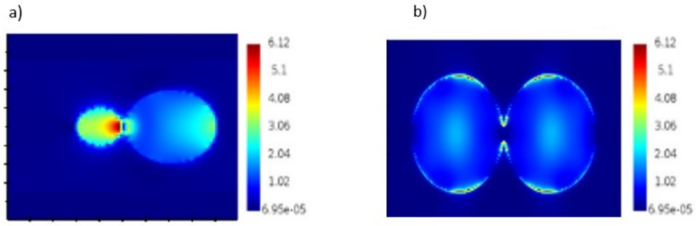

Figure 5.1: (a) FDTD field Enhancement of 200nm, 400nm ADNH (b) FDTD field Enhancement of 400nm hole diameter DNH.

sensitive and it has been shown that the detailed polarization analysis could determine the orientation of the DNHs. When the orientation is aligned parallel to the apex, minimal transmission occurs as the electromagnetic intensity is focused in the gap; conversely, maximum transmission is achieved with polarization orientated perpendicular to the apex [58]. The laser polarization direction was experimentally verified for ADNH by rotating a half wave plate (HWP) in front of the laser output, starting from the zero-order line of the HWP as was shown for DNH.[59].

Figure 5.2 (b) and (d) represent the transmission spectra for the parallel and perpendicular polarizations. The peak locations and intensities in the transmission spectra vary between the two polarizations, indicating that the ADNH structure interacts with light differently based on the polarization. However, at the specific wavelength of 980 nm, the transmission for both parallel and perpendicular polarizations shows minimal variation. This suggests that the nanostructure exhibits low polarization sensitivity at this wave-

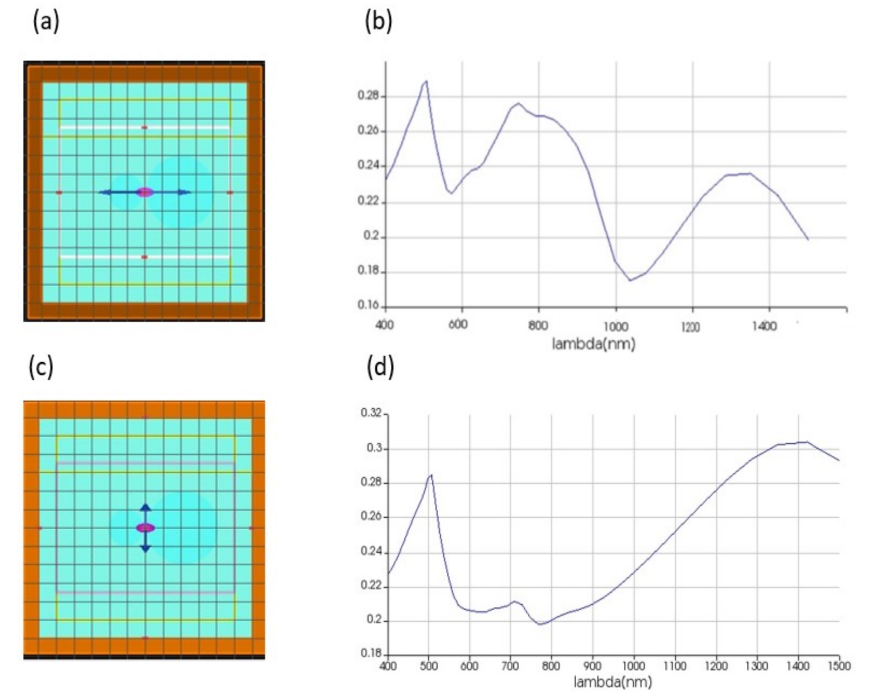

Figure 5.2: (a) FDTD simulation for parallel polarisation (b)Transmission spectra for parallel polarisation (c) FDTD simulation for perpendicular polarisation (d) Transmission spectra for perpendicular polarisation.

length.

5.4 Fabrication

5.4.1 Colloidal Lithography

As a first approach, we tried the down-to-top approach of colloidal lithography to fabricate ADNHs. This method is well explained in Chapter 1 of this thesis and is a well-proven, cost-effective method developed for the fabrication of regular DNHs. Polystyrene beads of two different sizes are chosen for preparing the solution. As per the simulations, the hole sizes should be 400 nm and 200 nm for tuning ADNHs for trapping at 980 nm wavelength laser. A solution is made by mixing 5μL of size 1 polystyrene beads and 5μL of size 2 polystyrene beads in 1 mL of ethanol solution. This solution is gently mixed by pipetting the solution up and down and also by gently rotating it to ensure that polystyrene beads are well dispersed in the ethanol solution. Using a pipette, 10 μL of this polystyrene-ethanol solution is deposited on each glass in a zig-zag pattern and left to dry overnight. 8 glass slides would be made each time like this as the sample plate on the MANTIS sputtering system can smoothly fit 8 slides. Once the coated slides are dried, they are plasma etched for different times to achieve ADNHs. The idea is to vary the polystyrene sizes and plasma etching times to reduce and remove the cusp between the regular DNHs. For this, polystyrene beads of 500 nm and 300 nm were tried first. The coated slides were plasma etched for 170 sec, 190 sec, 200 sec, 210 sec, 230 sec and 240 sec. After this, the coated slides sputtered with gold and the beads were removed by the process of sonication. Each glass slides were imaged using the Hitachi S-4800. Figure 5.3 shows the SEM image of ADNH from the 170 sec and 240 sec plasma etched coated slide. It can be observed that the cusp almost disappeared and the hole size also reduced below our requirement for the 240 sec plasma etched slide. The sizes of the holes were around only 300 nm and 130 nm. Similarly different Polystyrene beads were tried and the solution made by mixing 600 nm and 400 nm polystyrene beads looked promising. The coated slides were plasma-etched for different intervals between 200 sec and 320 sec. The slides etched for 310 sec had ADNHs close to the required size.

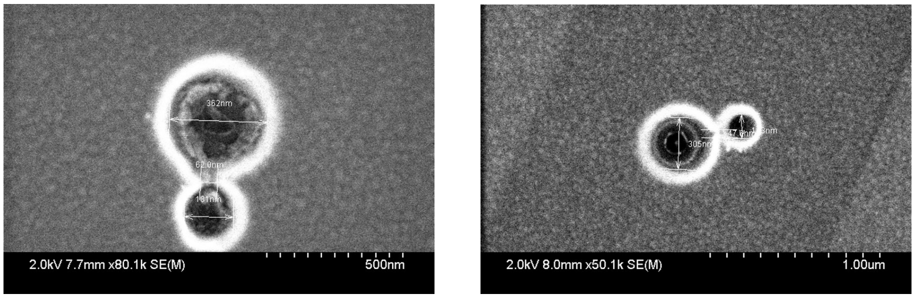

(a) (b)

Figure 5.3: ADNHs from 500 nm and 300 nm polystyrene coated glass slides plasma etched for (a) 170 sec and (b) 240 sec.

Another challenge with this method was locating the ADNH on the laser setup using CCD camera. Colloidal lithography intro-

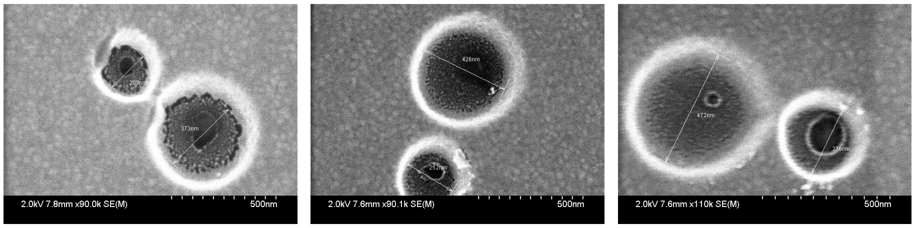

(a) (b) (c)

Figure 5.4: ADNHs from 600nm and 400nm polystyrene coated glass slides plasma etched for 320 sec.

duces many different structures on the slide, especially with two different polystyrene beads mixed. We were able to distinguish between clusters, single holes, and DNHs on the camera since larger apertures typically appear brighter because of longer wavelength cut-offs. However to distinguish between ADNHs that are partially detached and fully detached were difficult. Also, later it was found that ADNH looked similar to regular DNH on camera. One approach to overcome these challenges was drawing grids on the sample, numbering each grid, imaging the sample on SEM to find out the grids with ADNHs, constellation mapping and locating them on the camera. While constellation mapping proved effective for locating regular DNHs in our previous studies [60], it was not as efficient for ADNHs. This is primarily due to the lower number of ADNHs formed on the glass slide through the colloidal lithography method, compared to the number of regular DNHs we would get with the same method.

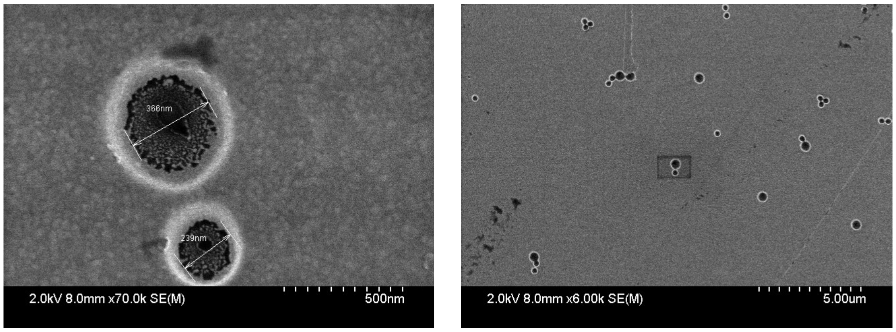

(a) (b)

Figure 5.5: ADNH and its corresponding constellation mapping.

5.4.2 Focused Ion Beam Milling

ADNHs were fabricated using the focused Ion Beam Milling technique. Regular DNHs were fabricated using the bit map mentioned in Chapter 1 of this Thesis. For ADNHs, bitmap wasn't used because the drilling time for the 200nm and 400nm nanoholes were different. The dwell time for 400nm hole was set to 24 sec and for the 200 nm hole, it was 12 se. The gap between the nanoholes was 80nm. These numbers were obtained after experimenting with different values. The size of the holes were also varied between +30 nm and -30nm until we could get the exact values.

Fiduciary markers were made on the gold slide to locate the holes both on SEM while imaging and on the laser setup for trapping. These markers were milled using an ion-accelerating voltage of 40 kV and a beam limiting aperture with a 520 μm diameter, under a 800k× magnification. The nanoholes were milled using a voltage of

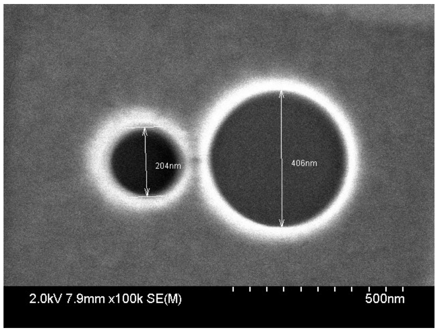

(a) ADNH using Focused Ion Beam Milling

40 kV and a beam-limiting aperture with a 5 μm diameter under 100k× magnification. Dwell Time, the time the ion beam spends on each point before moving to the next point was set to 10 μsec.

5.5 Experiments and Results

Plasmonic enhancement fields are launched by focusing a 980 nm wavelength laser onto the ADNH. A trapping solution was made by mixing 10 μL of 20 nm polystyrene in 0.5 mL of distilled water. The sample was made by putting 10 μL of this solution on the gold slide with ADNH and sealing it with a microscope slide. A linearly polarized trapping beam was focused normally onto the sample, in a polarization with the electric field yielding maximum transmission. The 20 nm polystyrene was trapped in the hotspots due to plasmonic field enhancement. The trap was also obtained at minimum polarisation, where the transmission through the ADNH is minimal. The power of the trap was varied to establish the relation between corner frequency and power at both minimum and maximum polarization. The results were compared with the trapping results of symmetric DNHs at both polarisations. protein trapping at different powers. The corner frequency is directly related to the stiffness of the trap.

Figure 5.7 shows the trapping results from ADNH and DNHs. The symmetric DNH demonstrates consistently higher corner frequencies at both maximum and minimum polarizations when compared to the ADNH at comparable laser currents. This indicates that the symmetric DNH offers a more robust and stable trapping environment. The likely cause of this is the more uniform electric field distribution within the symmetric structure, leading to more effective confinement of the trapped particles. Additionally, the broader variation in corner frequencies in the symmetric DNH suggests a higher sensitivity to changes in polarization. However, this also indicates a stronger overall trapping capability at the same laser currents, potentially making the symmetric DNH more efficient for trapping across varying conditions. On the other hand, the ADNH shows a narrower range of corner frequencies between different polarizations, suggesting that polarization has a less pronounced effect on the trapping strength in this case. This observation aligns with the results obtained from the FDTD simulation, reinforcing the conclusion that

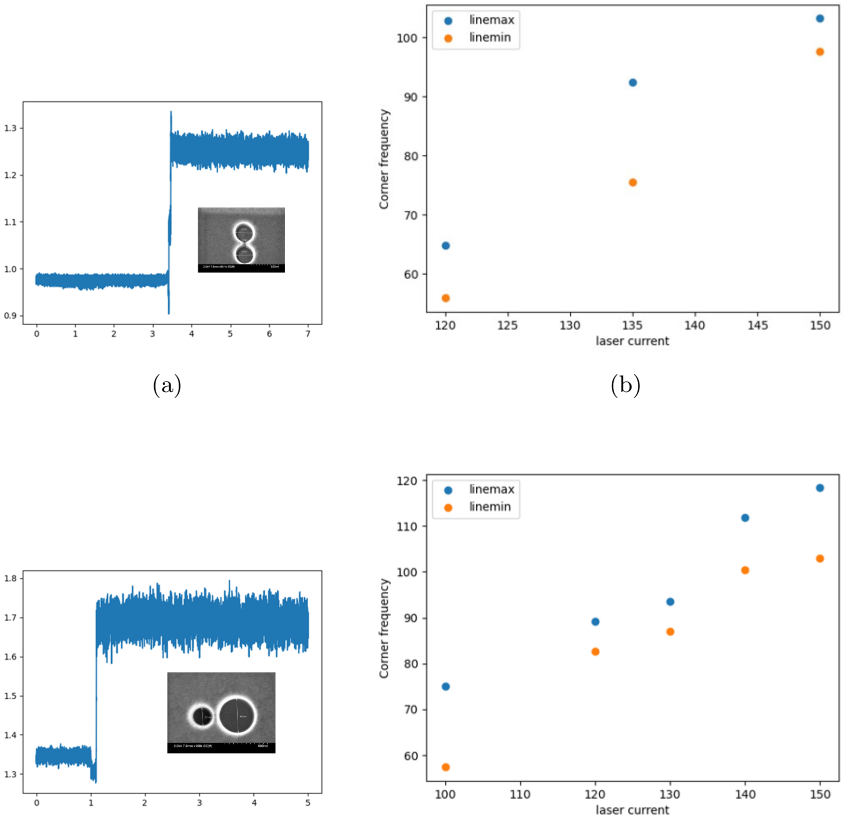

(a) (b)

(c) (d)

Figure 5.7: (a) Trap Signal of 30nm PS on regular DNH. The inlet shows DNH. (b) Corner Frequency vs Laser current for Regular DNH. The blue and orange dots are corner frequencies at maximum and minimum polarization respectively (c) Trap Signal of 30nm PS on ADNH. The inlet shows ADNH. (d) Corner Frequency vs Laser current for ADNH.

the ADNH structure exhibits low polarization sensitivity at the 980 nm wavelength. Additionally, significant variations in transmission were observed at different wavelengths, suggesting that further investigation into the performance of the ADNH structure across a broader spectrum would be valuable.

5.6 Concluding Remarks

This chapter investigated a novel nanostructure, the ADNHs, to assess whether it offers improved performance compared to traditional DNHs. The effect of laser polarization on ADNHs was studied and compared with that of symmetric DNHs. Additionally, 30 nm polystyrene beads were optically trapped on both ADNHs and DNHs under varying laser powers and at both minimum and maximum polarization. The results suggest that ADNHs perform similarly to regular DNHs, with no significant improvement, and in some cases may even be less efficient for trapping.

Chapter 6

Classification of Lipopolysaccharides using DNH Optical Tweezers: Ongoing project.

6.1 Introduction

Bacterial infections, typically resulting from either Gram-positive or Gram-negative bacteria, provide significant threats to human health. Notorious pathogens among Gram-negative bacteria are responsible for severe illnesses, including meningitis, pneumonia, diarrhea, and plague. A crucial element in the detrimental effects of Gram-negative bacteria is the presence of lipopolysaccharides (LPS), commonly referred to as endotoxins. LPS are powerful inflammatory chemicals located on the outer membrane of these bacteria. They may be released during bacterial cell division or upon the destruction of bacteria, such as through antibiotics. Excessive release of LPS into the bloodstream can provoke a severe inflammatory response, potentially resulting in septic shock, organ failure, and mortality. Conversely, in diminished quantities, LPS can activate the immune system, augmenting the host's immunological response. The dual character of LPS—potentially harmful or advantageous based on concentration—remains a subject of intrigue for scientists, as enhanced comprehension of these molecules may reveal novel approaches for disease prevention and immune system regulation [61].

LPS consist of three separate sections. Lipid A is a glycophospholipid that secures LPS to the bacterial membrane. Lipid A is highly hydrophobic and accounts for the majority of the biological effects associated with LPS, making it the endotoxically active constituent. Lipid A is generally linked to a core oligosaccharide through an acidic sugar known as 2-keto-3-deoxy-octulosonic acid (Kdo). The third component of LPS, the O-chain, comprises repetitive oligosaccharide units that project outward from the bacterial surface. The O-specific chain is distinctive to each bacterial species and serves as the foundation for serotyping, a technique traditionally employed to differentiate various strains of Gram-negative bacteria [62].

The Limulus amoebocyte lysate (LAL) test is the most widely used and recognized method for detecting endotoxins. Despite its widespread

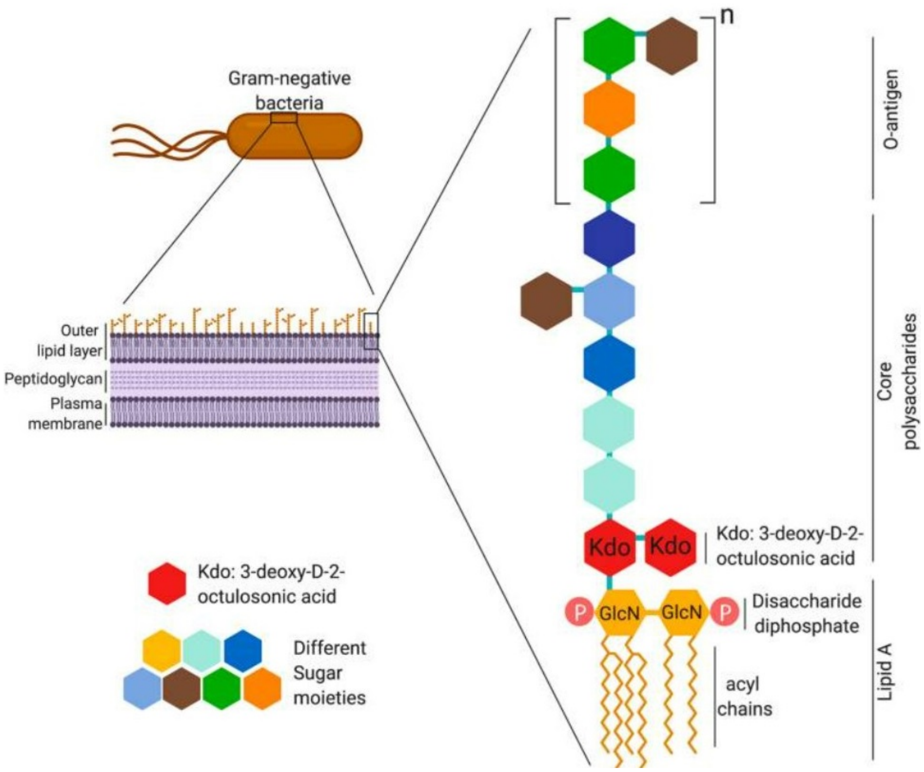

Figure 6.1: Structure of LPS showing Lipid A, Core oligosaccharide and O-antigen. Figure adapted from [63]

adoption in the biopharmaceutical industry, there remains room for improvement in the LAL assay [64]. Alternative methods that do not rely on LAL reagents have been developed, including optical [65] [66], thermal [67], and electrochemical sensors [68]. Additionally, various affinity molecules such as proteins [69], peptides [70], and others [71] are being explored for their potential in LPS detection. In this chapter, I present ongoing research focused on detecting single LPS molecules and distinguishing between various types of LPS using DNH optical tweezers. The study aims to analyze four LPS species however, at this stage, only the results from two species have been included in the thesis, as data collection for the remaining species is still in progress. Further experimentation and analysis are required to complete the study.

6.2 Methods

The LPS, Escherichia coli O55:B5, Klebsiella pneumoniae, Pseudomonas aeruginosa and Salmonella enterica from typhimurium are purchased from Sigma Aldrich. These LPS are prepared at a concentration of 0.1 wt/v % by weighing them in 1.5 μL Eppendorf tubes. Distilled water is used as solvent for the experiment. The diluted LPS is sonicated for 3-5 minutes and centrifuged at 13000 rpm for 10 minutes before using it for trapping.

A 980nm wavelength laser was focused on the DNH to introduce plasmonic enhancements on the cusp of the DNH, to trap LPS. The sample used for trapping had DNHs with 500nm diameter holes and an average cusp size of 35nm. The LPS were trapped at a laser current of 100mA which gave 9.8 mW of laser power after the 100× objective.

6.3 Experiments and Results

As shown in Chapter 2 of this thesis, the RMS of transmission signal intensity will scale with polarizability, which scales with particle volume(r^3), resulting in a linear dependence with molecular weight. The RMSD of the trapped data was calculated for two LPS, E. coli and S. enterica, and shows a dependence on its molecular weight. The molecular weight of the LPS in this experiment is given in Table 6.1.

LPS	Mw(g/mol)
E. coli B5	82.1×10^3
S. typhimurium	63.1×10^3
K. pneumoniae	21.4×10^3
P. aeruginosa	7.3×10^3

Table 6.1: Molecular Weight of LPS used in the study [66].

The trapping result of E-coli and S. enterica are shown in Figure 6.2. The RMS value of the trapped signal for E. coli (0.0104) is greater than that of S. enterica (0.009), indicating a linear relationship with their molecular weights. Additionally, the corner frequencies of the traps, which reflect the stiffness of the optical traps, were calculated. E. coli exhibited a corner frequency of 62.4 Hz, while S. enterica showed a corner frequency of 45.5 Hz. These results also support a linear correlation between corner frequency and particle size. However, further data collection and analysis are needed to

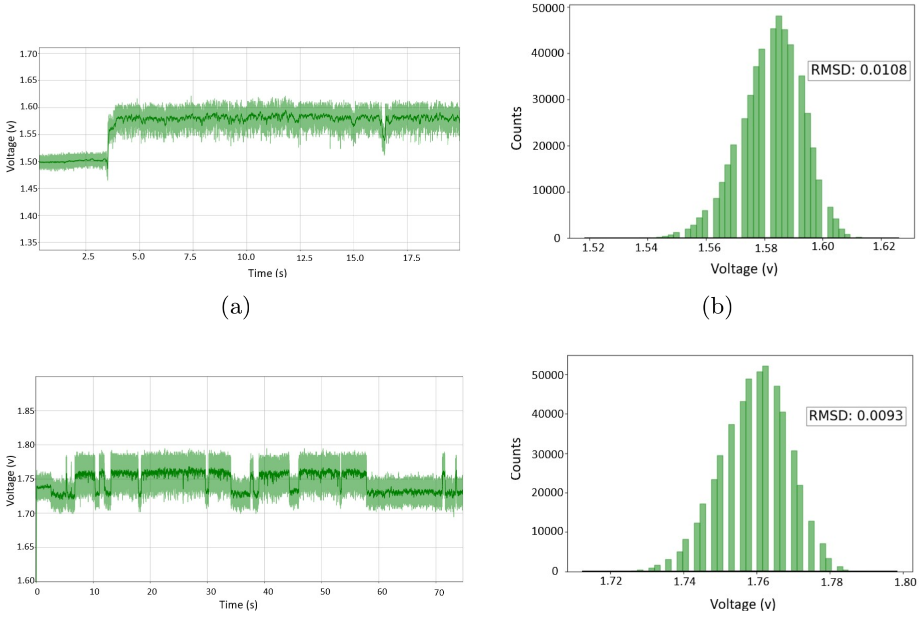

(a) (b)

(c) (d)

Figure 6.2: (a) Optical Trapping Signal of E.coli (b) RMSD of the E.coli trapped signal (c) Optical Trapping signal of S.enterica (d) RMSD of the S.enterica trapped signal.

reinforce these findings. The change in transmission observed in the trapped signal of S. enterica (Figure 6.2:(c)) is also noteworthy; however, it falls outside the current scope of this discussion.

6.4 Concluding Remarks

This chapter provided an overview of ongoing research focused on the classification of various LPS using DNH optical tweezers. While results from two LPS types are presented here, additional work is ongoing to further explore and analyze other LPS.

Chapter 7

Conclusions and Future Works

Chapter 2 of this thesis explains the theory of plasmonics, optical tweezers, and subwavelength apertures, demonstrating the superiority of DNH tweezers in trapping applications compared to traditional optical tweezers.. It also provides a detailed analysis of the trapping efficiency and stiffness of the DNH optical trap, quantifying these properties to demonstrate the superior performance of the DNH system compared to traditional optical tweezers. Chapter 3 explained the fabrication procedures for DNH with a detailed explanation of the OT setup. The experimental study in Chapter 4 explored the conformational dynamics of individual, unaltered BSA molecules utilizing DNH tweezers. The Gibbs energy for the N to F states was calculated for both labeled and Unlabelled BSA from the free energy diagram and the values show a small effect of labeling on BSA. This Chapter also explored the effect of electrostatic interactions between the gold surface and proteins with different charges on the trapping process. The study was conducted on three proteins: BSA, CA, and CTC. In the future, polystyrene beads at different salt concentrations (NaCl, KCl) could be studied which would provide a more controlled and systematic way to understand the electrostatic interactions in an optical trap. In Chapter 5 of the thesis, a novel nanostructure, ADNHs was explored. Their fabrication process and a detailed analysis of variation in corner frequencies at different powers for regular DNH and ADNH were conducted. However, the ADNH structures did not demonstrate a significant improvement in trapping performance compared to the regular DNH. A future work related to this study would be to adjust the size and shape of the holes to fine-tune the resonance frequencies to target specific particles or molecules which allows for the possibility of multi-frequency trapping or multi-wavelength sensing. Moreover, the FDTD simulation revealed significant variations in transmission across different wavelengths, indicating that further exploration of the ADNH structure's performance over a broader spectral range would be worthwhile. Chapter 6 presented an overview of the ongoing research aimed at classifying various LPS using DNH optical tweezers. Although this chapter highlights findings from two specific types of LPS, further investigations are in progress to extend the analysis to four different LPS molecules.

Bibliography

[1] A. Ashkin. “Acceleration and Trapping of Particles by Radiation Pressure”. In: *Phys. Rev. Lett.* 24 (4 Jan. 1970), pp. 156–159.

[2] A. Ashkin et al. “Observation of a single-beam gradient force optical trap for dielectric particles”. In: *Opt. Lett.* 11.5 (May 1986), pp. 288–290.

[3] A. Ashkin, J. M. Dziedzic, and T. Yamane. “Optical trapping and manipulation of single cells using infrared laser beams”. In: *Nature* 330.6150 (Dec. 1987), pp. 769–771. ISSN: 1476-4687.

[4] A Ashkin and J M Dziedzic. “Optical trapping and manipulation of viruses and bacteria”. en. In: *Science* 235.4795 (Mar. 1987), pp. 1517–1520.

[5] Keir C Neuman and Steven M Block. “Optical trapping”. en. In: *Rev. Sci. Instrum.* 75.9 (Sept. 2004), pp. 2787–2809.

[6] Yasuhiro Harada and Toshimitsu Asakura. “Radiation forces on a dielectric sphere in the Rayleigh scattering regime”. In: *Optics Communications* 124.5 (1996), pp. 529–541. ISSN: 0030-4018.

[7] Silvia Albaladejo et al. “Scattering Forces from the Curl of the Spin Angular Momentum of a Light Field”. In: *Phys. Rev. Lett.* 102 (11 Mar. 2009), p. 113602.

[8] Susan E. Skelton Spesyvtseva and Kishan Dholakia. “Trapping in a Material World”. In: *ACS Photonics* 3.5 (May 2016), pp. 719–736.

[9] Bruce T Draine. “The discrete-dipole approximation and its application to interstellar graphite grains”. In: *Astrophysical Journal, Part 1 (ISSN 0004-637X), vol. 333, Oct. 15, 1988, p. 848-872.* 333 (1988), pp. 848–872.

[10] Domna G. Kotsifaki and Síle Nic Chormaic. In: *Nanophotonics* 8.7 (2019), pp. 1227–1245.

[11] Pablo Purohit et al. “Optical trapping reveals differences in dielectric and optical properties of copper nanoparticles compared to their oxides and ferrites”. en. In: *Sci. Rep.* 10.1 (Jan. 2020), p. 1198.

[12] Lukas Novotny, Randy X. Bian, and X. Sunney Xie. “Theory of Nanometric Optical Tweezers”. In: *Phys. Rev. Lett.* 79 (4 July 1997), pp. 645–648.

[13] Philipp Bechtluft et al. “Direct Observation of Chaperone-Induced Changes in a Protein Folding Pathway”. In: *Science* 318.5855 (2007), pp. 1458–1461.

[14] A Mossa et al. “Dynamic force spectroscopy of DNA hairpins: I. Force kinetics and free energy landscapes”. In: *Journal of Statistical Mechanics: Theory and Experiment* 2009.02 (Feb. 2009), P02060.

[15] M Caldarini et al. “The complex folding behavior of HIV-1-protease monomer revealed by optical-tweezer single-molecule experiments and molecular dynamics simulations”. en. In: *Biophys. Chem.* 195 (Dec. 2014), pp. 32–42.

[16] H. A. Bethe. “Theory of Diffraction by Small Holes”. In: *Phys. Rev.* 66 (7-8 Oct. 1944), pp. 163–182.

[17] T. W. Ebbesen et al. “Extraordinary optical transmission through subwavelength hole arrays”. In: *Nature* 391.6668 (Feb. 1998), pp. 667–669. ISSN: 1476-4687.

[18] Reuven Gordon and Alexandre G. Brolo. “Increased cut-off wavelength for a subwavelength hole in a real metal”. In: *Opt. Express* 13.6 (Mar. 2005), pp. 1933–1938.

[19] Yuquan Zhang et al. “Plasmonic tweezers: for nanoscale optical trapping and beyond”. In: *Light: Science & Applications* 10.1 (Mar. 2021), p. 59. ISSN: 2047-7538.

[20] Cecilia Noguez. “Surface Plasmons on Metal Nanoparticles: The Influence of Shape and Physical Environment”. In: *The Journal of Physical Chemistry C* 111.10 (Mar. 2007), pp. 3806–3819. ISSN: 1932-7447.

[21] Amr A. E. Saleh and Jennifer A. Dionne. "Toward Efficient Optical Trapping of Sub-10-nm Particles with Coaxial Plasmonic Apertures". In: *Nano Letters* 12.11 (Nov. 2012), pp. 5581–5586. ISSN: 1530-6984.

[22] Kai Wang et al. "Trapping and rotating nanoparticles using a plasmonic nano-tweezer with an integrated heat sink". en. In: *Nat. Commun.* 2.1 (Sept. 2011), p. 469.

[23] Mathieu L. Juan et al. "Self-induced back-action optical trapping of dielectric nanoparticles". In: *Nature Physics* 5.12 (Dec. 2009), pp. 915–919. ISSN: 1745-2481.

[24] Yuanjie Pang and Reuven Gordon. "Optical Trapping of 12 nm Dielectric Spheres Using Double-Nanoholes in a Gold Film". In: *Nano Letters* 11.9 (Sept. 2011), pp. 3763–3767. ISSN: 1530-6984.

[25] Yuanjie Pang and Reuven Gordon. "Optical Trapping of a Single Protein". In: *Nano Letters* 12.1 (Jan. 2012), pp. 402–406. ISSN: 1530-6984.

[26] Skyler Wheaton and Reuven Gordon. "Molecular weight characterization of single globular proteins using optical nanotweezers". In: *Analyst* 140 (14 2015), pp. 4799–4803.

[27] Veerpal Kaur et al. "Portable fiber-based double nanohole optical tweezer for trapping small proteins". In: *Journal of Physics: Photonics* 6.3 (July 2024), p. 035023.

[28] Ana Zehtabi-Oskuie et al. "Double nanohole optical trapping: dynamics and protein-antibody co-trapping". In: *Lab Chip* 13 (13 2013), pp. 2563–2568.

[29] Abhay Kotnala and Reuven Gordon. "Double nanohole optical tweezers visualize protein p53 suppressing unzipping of single DNA-hairpins". In: *Biomedical optics express* 5.6 (2014), pp. 1886–1894.

[30] Frederick Gittes and Christoph F Schmidt. "Signals and noise in micromechanical measurements". In: *Methods in cell biology* 55 (1997), pp. 129–156.

[31] Abhay Kotnala and Reuven Gordon. "Quantification of High-Efficiency Trapping of Nanoparticles in a Double Nanohole Optical Tweezer". In: *Nano Letters* 14.2 (Feb. 2014), pp. 853–856. ISSN: 1530-6984.

[32] Mathew Peters. "Label-Free Studies of Single Biological Nanoparticles Using Optical Nanotweezers". Master's Thesis. MA thesis. University of Victoria, 2024.

[33] John D. Harvey, Robert Geddes, and Peter R. Wills. "Conformational studies of BSA using laser light scattering". In: *Biopolymers* 18.9 (1979), pp. 2249–2260. ISSN: 0006-3525.

[34] T Kosa, T Maruyama, and M Otagiri. "Species differences of serum albumins: I. Drug binding sites". en. In: *Pharm Res* 14.11 (Nov. 1997), pp. 1607–1612.

[35] MK Quinn et al. "How fluorescent labelling alters the solution behaviour of proteins". In: *Physical Chemistry Chemical Physics* 17.46 (2015), pp. 31177–31187.

[36] P J Sadler and A Tucker. "pH-induced structural transitions of bovine serum albumin. Histidine pKa values and unfolding of the N-terminus during the N to F transition". en. In: *Eur J Biochem* 212.3 (Mar. 1993), pp. 811–817.

[37] Liujiao Bian, Dan Wu, and Wei Hu. "Temperature-induced conformational transition of bovine serum albumin in neutral aqueous solution by reversed-phase liquid chromatography". en. In: *Biomed Chromatogr* 28.2 (Aug. 2013), pp. 295–301.

[38] Paulina Tworek et al. "Changes in Secondary Structure and Properties of Bovine Serum Albumin as a Result of Interactions with Gold Surface". en. In: *Chemphyschem* 25.2 (Dec. 2023), e202300505.

[39] Vibhor Mishra and Richard J Heath. "Structural and Biochemical Features of Human Serum Albumin Essential for Eukaryotic Cell Culture". en. In: *Int J Mol Sci* 22.16 (Aug. 2021).

[40] Larnii S. Booth et al. "Modelling of the dynamic polarizability of macromolecules for single-molecule optical biosensing". In: *Scientific Reports* 12.1 (Feb. 2022), p. 1995. ISSN: 2045-2322.

[41] Quanbo Jiang et al. "Quantifying the Role of the Surfactant and the Thermophoretic Force in Plasmonic Nano-optical Trapping". In: *Nano Letters* 20.12 (Dec. 2020), pp. 8811–8817. ISSN: 1530-6984.

[42] Quanbo Jiang et al. "Temperature Measurement in Plasmonic Nanoapertures Used for Optical Trapping". In: *ACS Photonics* 6.7 (July 2019), pp. 1763–1773.

[43] Cuifeng Ying et al. *Watching Single Unmodified Enzymes at Work*. 2021. arXiv: `2107.06407 [physics.bio-ph]`.

[44] Zhe Xu, Wuzhou Song, and Kenneth B. Crozier. "Direct Particle Tracking Observation and Brownian Dynamics Simulations of a Single Nanoparticle Optically Trapped by a Plasmonic Nanoaperture". In: *ACS Photonics* 5.7 (July 2018), pp. 2850–2859.

[45] Yexuan Mao et al. "A novel method for the study of molecular interaction by using microscale thermophoresis". In: *Talanta* 132 (2015), pp. 894–901. ISSN: 0039-9140.

[46] Manuela E Richert, Natalia García Rey, and Björn Braunschweig. "Charge-Controlled Surface Properties of Native and Fluorophore-Labeled Bovine Serum Albumin at the Air–Water Interface". In: *J. Phys. Chem. B* 122.45 (Nov. 2018), pp. 10377–10383.

[47] Matthew Peters, Tianyu Zhao, Sherin George, et al. "Energy Landscape of Conformational Changes for a Single Unmodified Protein". In: *Research Square* (Sept. 2024). Preprint (Version 1).

[48] Felix Ameseder et al. "Localised contacts lead to nanosecond hinge motions in dimeric bovine serum albumin". In: *Phys. Chem. Chem. Phys.* 21 (34 2019), pp. 18477–18485.

[49] Maik Hüttemann et al. "The multiple functions of cytochrome c and their regulation in life and death decisions of the mammalian cell: From respiration to apoptosis". en. In: *Mitochondrion* 11.3 (May 2011), pp. 369–381.

[50] J B Feldstein and D N Silverman. "Purification and characterization of carbonic anhydrase from the saliva of the rat". en. In: *J. Biol. Chem.* 259.9 (May 1984), pp. 5447–5453.

[51] Qinghong Shi, Ying Zhou, and Yan Sun. "Influence of pH and Ionic Strength on the Steric Mass-Action Model Parameters around the Isoelectric Point of Protein". In: *Biotechnology Progress* 21.2 (2005), pp. 516–523.

[52] Eun-Soo Kwak et al. "Optical Trapping with Integrated Near-Field Apertures". In: *The Journal of Physical Chemistry B* 108.36 (Sept. 2004), pp. 13607–13612. ISSN: 1520-6106.

[53] Mathieu L. Juan, Maurizio Righini, and Romain Quidant. "Plasmon nano-optical tweezers". In: *Nature Photonics* 5.6 (June 2011), pp. 349–356. ISSN: 1749-4893.

[54] Ahmed A Al Balushi and Reuven Gordon. "A label-free untethered approach to single-molecule protein binding kinetics". In: *Nano letters* 14.10 (2014), pp. 5787–5791.

[55] Tatsuya Shoji et al. "Permanent fixing or reversible trapping and release of DNA micropatterns on a gold nanostructure using continuous-wave or femtosecond-pulsed near-infrared laser light". In: *Journal of the American Chemical Society* 135.17 (2013), pp. 6643–6648.

[56] Reuven Gordon. "Double Nanohole Aperture Optical Trapping". In: *Optics in the Life Sciences.* Optica Publishing Group, 2013, TT1D.1.

[57] TY - JOUR AU - Yu et al. "Yuanjie C7-2202924 TI - Boosting Trapping in Dark Mode and Emission in Bright Mode using a Quad-Nanohole JO - Advanced Optical Materials JA - Adv". In: *It is experimentally demon-*

strated that the photoluminescence of the UCNP optically trapped in the quad-nanohole is enhanced by a factor of 87 (as compared to a UCNP trapped in the single nanohole), and this enhancement factor surpasses that from a bowtie nanohole?one of the ?gold standards? for local field enhancement of (2023). Ed. by A quad-nanohole structure with two bright-field modes for enhanced excitation and as well as a dark-field mode for enhanced optical trapping is emission of the UCNP.

[58] Raju Regmi et al. "Nanoscale volume confinement and fluorescence enhancement with double nanohole aperture". In: *Scientific Reports* 5.1 (Oct. 2015), p. 15852. ISSN: 2045-2322.

[59] Ghazal Hajisalem et al. "Accessible high-performance double nanohole tweezers". In: *Opt. Express* 30.3 (Jan. 2022), pp. 3760–3769.

[60] Adarsh Lalitha Ravindranath et al. "Colloidal lithography double-nanohole optical trapping of nanoparticles and proteins". In: *Opt. Express* 27.11 (May 2019), pp. 16184–16194.

[61] Martine Caroff and Alexey Novikov. "Lipopolysaccharides: structure, function and bacterial identifications". In: *OCL* 27 (2020), p. 31.

[62] Clett Erridge, Elliott Bennett-Guerrero, and Ian R. Poxton. "Structure and function of lipopolysaccharides". In: *Microbes and Infection* 4.8 (2002), pp. 837–851. ISSN: 1286-4579.

[63] Lalita Mazgaeen and Prajwal Gurung. "Recent Advances in Lipopolysaccharide Recognition Systems". en. In: *Int J Mol Sci* 21.2 (Jan. 2020).

[64] Yuan Cao, Yujie Zhang, and Frank Qiu. "Low endotoxin recovery and its impact on endotoxin detection". en. In: *Biopolymers* 112.11 (Nov. 2021), e23470.

[65] Radhika N K and Sai Siva Gorthi. "dsDNA-templated fluorescent copper nanoparticles for the detection of lipopolysaccharides". en. In: *Anal. Methods* 13.2 (Jan. 2021), pp. 186–191.

[66] Rui Zhu et al. “Single-molecule lipopolysaccharides identification and the interplay with biomolecules via nanopore readout”. en. In: *Biosens. Bioelectron.* 240.115641 (Nov. 2023), p. 115641.

[67] E Eduardo Antunez et al. “A regenerable biosensing platform for bacterial toxins”. en. In: *Biomacromolecules* 22.2 (Feb. 2021), pp. 441–453.

[68] Yue Huang et al. “Highly sensitive detection of lipopolysaccharide based on collaborative amplification of dual enzymes”. en. In: *Anal. Chim. Acta* 1126 (Aug. 2020), pp. 31–37.

[69] Ghulam Murtaza et al. “Glycated albumin based photonic crystal sensors for detection of lipopolysaccharides and discrimination of Gram-negative bacteria”. en. In: *Anal. Chim. Acta* 1117 (June 2020), pp. 1–8.

[70] Apurva Panjla et al. “Short peptides and their mimetics as potent antibacterial agents and antibiotic adjuvants”. en. In: *ACS Chem. Biol.* 16.12 (Dec. 2021), pp. 2731–2745.

[71] Yueshuang Xu et al. “Aptamer-based hydrogel barcodes for the capture and detection of multiple types of pathogenic bacteria”. en. In: *Biosens. Bioelectron.* 100 (Feb. 2018), pp. 404–410.